Predicting the three-dimensional age-depth field of an ice rise

A. Clara J. Henry[1], Clemens Schannwell[1], Vjeran Višnjević[2], Joanna Millstein[3], Paul D Bons[4], Olaf Eisen[5], and Reinhard Drews[6]

[1]Max Planck Institute for Meteorology
[2]University of Tübingen
[3]Massachusetts Institute of Technology
[4]Universität Tübingen
[5]Alfred Wegener Institute Helmholtz Center for Polar and Marine Research
[6]Department of Geosciences, University of Tübingen

August 17, 2023

Abstract

Ice rises situated around the perimeter of Antarctica buttress ice flow and contain information about the past climate and changes in flow regime. Moreover, ice rises contain convergent and divergent flow regimes, and both floating and grounded ice over comparatively small spatial scales, meaning they are ideal locations to study ice-flow dynamics. Here, we introduce a new modelling framework that permits the comparison between modelled and observed stratigraphy. A thermo-mechanically coupled, isotropic, full Stokes ice flow model with a dynamic grounding line is used (Elmer/Ice). The result is the simulated age-depth field of a three-dimensional, steady-state ice rise which is dynamically coupled to the surrounding ice shelf. Applying the model to Derwael Ice Rise, results show a good match between observed and modelled stratigraphy over most of the ice rise and predict approximately 8000 year old ice at a depth of 95 \%. Differences in the prediction of age between simulations using Glen's flow law exponents of $n=3$ and $n=4$ are generally small (<5 \% over most areas). In the ice rise shear zones, large differences in shear strain rates in the velocity direction are found between the $n=3$ and the $n=4$ simulations. Our simulations indicate that a Glen's flow law exponent of $n=4$ may be better suited when modelling ice rises due to a steady-state geometry which is closer to the observed geometry. Our three-dimensional modelling framework can easily be transferred to other ice rises and has relevance for researchers interested in ice core dating and understanding ice-flow re-organisation.

Predicting the three-dimensional age-depth field of an ice rise

A. C. J. Henry[1,2,3], C. Schannwell[1], V. Višnjević[2], J. Millstein[4], P. D. Bons[2], O. Eisen[5,6], R. Drews[2]

[1]Max Planck Institute for Meteorology, Hamburg, Germany
[2]Department of Geosciences, University of Tübingen, Tübingen, Germany
[3]International Max Planck Research School on Earth System Modelling, Max Planck Institute for Meteorology, Hamburg, Germany
[4]Massachusetts Institute of Technology—Woods Hole Oceanographic Institute Joint Program in Oceanography/Applied Ocean Science and Engineering, Cambridge, MA, USA
[5]Alfred Wegener Institute Helmholtz Centre for Polar and Marine Research, Bremerhaven, Germany
[6]University of Bremen, Bremen, Germany

Key Points:

- First three-dimensional simulations of the stratigraphy of an ice rise allowing comparison of model results with radar observations.
- Choice of the Glen's flow law exponent influences deformation in the grounding zones.
- Reduction in surface elevation at the divide relative to observations points at missing processes in the model such as anisotropy.

Corresponding author: A. C. J. Henry, `clara.henry@mpimet.mpg.de`

Abstract

Ice rises situated around the perimeter of Antarctica buttress ice flow and contain information about the past climate and changes in flow regime. Moreover, ice rises contain convergent and divergent flow regimes, and both floating and grounded ice over comparatively small spatial scales, meaning they are ideal locations to study ice-flow dynamics. Here, we introduce a new modelling framework that permits the comparison between modelled and observed stratigraphy. A thermo-mechanically coupled, isotropic, Stokes ice flow model with a dynamic grounding line is used (Elmer/Ice). The result is the simulated age-depth field of a three-dimensional, steady-state ice rise which is dynamically coupled to the surrounding ice shelf. Applying the model to Derwael Ice Rise, results show a good match between observed and modelled stratigraphy over most of the ice rise and predict approximately 8000 year old ice at a depth of 95 %. Differences in the prediction of age between simulations using Glen's flow law exponents of $n = 3$ and $n = 4$ are generally small (< 5 % over most areas). In the ice rise shear zones, large differences in shear strain rates in the velocity direction are found between the $n = 3$ and the $n = 4$ simulations. Our simulations indicate that a Glen's flow law exponent of $n = 4$ may be better suited when modelling ice rises due to a steady-state geometry which is closer to the observed geometry. Our three-dimensional modelling framework can easily be transferred to other ice rises and has relevance for researchers interested in ice core dating and understanding ice-flow re-organisation.

Plain Language Summary

Ice rises are features which form in coastal Antarctica when the ice shelf comes into contact with the bathymmetry. These features provide a backstress on the ice shelf and can influence grounding line position. We simulate an ice rise in East Antarctica called Derwael Ice Rise, outlining the steps necessary to model the three-dimensional stratigraphy of an ice rise and compare the modelled stratigraphy with observed stratigraphy derived from radar measurements. Comparisons between the observed and modelled stratigraphy allow us to validate boundary conditions and the parameterisations used in our model. This work is relevant as a blueprint for simulating other ice rises for those interested in comparison with ice core records, and investigating ice rises formation and evolution.

1 Introduction

Ice rises form where ice shelves ground locally on topographic highs in the bathymetry and are important in coastal Antarctic ice flow dynamics as they regulate the flow of ice towards the ocean (Favier & Pattyn, 2015; Favier et al., 2016; Henry et al., 2022). Moreover, ice rises are valuable as a climate archive because they often provide high-resolution and undisturbed records throughout the Holocene. Ice-core drill sites are often located at local summits to avoid lateral flow. However, it is a significant challenge to predict the age-depth fields prior to drilling. This is due to strong variations in surface mass balance (SMB, Cavitte et al. (2022)) and also because the ice-flow regimes change over a few tens of kilometres. Divide flow at the summit (where arches in the internal stratigraphy may form) turns into flank flow, and finally to the grounding zone where coupling with the surrounding ice shelves takes place. Compared to Antarctica's interior, ice rises at the coast are comparatively easy to reach and consequently a number of them , Derwael Ice Rise being one of them, have been densely surveyed with radar to image the isochronal stratigraphy. This enables the comparison of model predictions across various flow regimes with observations which can help calibrate model parameters such as Glen's flow law exponent, the fundamental constitutive relation for ice flow.

The non-Newtonian flow of ice (J. W. Glen, 1955; Weertman, 1983; Budd & Jacka, 1989) results in Raymond arches (Raymond, 1983) which form in the stratigraphy under the ice-rise divides and have been used to estimate how stationary ice-divide flow is. This effect can be dampened, for example, by along-ridge flow or changing conditions, thus inhibiting their formation. Under a changing climate, the geometry of an ice rise often changes, thereby causing a change in the isochronal structure (Nereson et al., 1998; Martín et al., 2009). The onset of stability of an ice rise is indicated by the amplitude of the Raymond arches and a change in the size of an ice rise is indicated by the migration of Raymond arches visible in the stratigraphy as side arches or tilted anticline stacks. Simulations of the stratigraphy of specific ice rises have thus far been performed in two dimensions (Martín et al., 2006, 2009, 2014; Drews et al., 2015; Goel et al., 2018), with Gillet-Chaulet and Hindmarsh (2011) performing simulations of the stratigraphy of an idealised ice rise in three dimensions without the inclusion of the surrounding ice shelf.

In this paper, we build on previous ice-rise modelling studies (Martín et al., 2009; Drews et al., 2015; Schannwell et al., 2019, 2020) and extend them by introducing a modelling framework that allows us to model ice rises including the surrounding ice shelves and their stratigraphy in three dimensions. This not only permits the prediction of the stratigraphy, but also accounts for three-dimensional effects that are of importance for comparisons with radar observations and ice cores. Whilst having proven important in the development of an understanding of Raymond arches, the two-dimensional studies do not allow for along-ridge flow. Studies investigating the observed stratigraphy in shear zones (Franke et al., 2022) and zones of convergence (Bons et al., 2016) have been performed, but a comparison between observed and modelled stratigraphy in such settings has not yet been performed. In idealised simulations (Hindmarsh et al., 2011; Gillet-Chaulet et al., 2011), it has been shown that along-ridge flow has a dampening effect on Raymond arch evolution. Where these simulations lack, however, is in the use of idealised boundary forcing conditions, which do not sufficiently produce the differing flow regime conditions on the stoss and lee sides of an ice rise.

The introduction of our new modelling framework provides a blueprint for modelling a real-world ice rise in three dimensions using the thermo-mechanically coupled model Elmer/Ice (Gagliardini et al., 2013) in order to predict the age field ice-rise wide. We investigate how robust those results are compared to observations with two Glen's flow law exponents. We choose to compare simulations using the typical exponent of $n = 3$ with simulations using an exponent of $n = 4$, closer to the value of $n = 4.1 \pm 0.4$ found to work best for Antarctic ice shelves (Millstein et al., 2022) and similar values suggested by Bons et al. (2018) for Greenland. The conversion from using a Glen's flow law with an exponent of $n = 3$ to an exponent of $n = 4$ is made using an initial scalar stress estimate along with simulations for the evaluation of an appropriate Arrhenius prefactor for $n = 4$.

The three-dimensional, steady-state simulations presented here have relevance for comparisons with ice cores and in the context of understanding the link between isochronal structures and changes in ice geometry and external forcing. Steady-state simulations allow the deduction of changes due to misfits and provide an important step towards the use of ice rises as a constraint for paleo ice-sheet simulations. This study not only successfully demonstrates three-dimensional modelling to bridge Stokes models with observed radar stratigraphy, but also delves into the implications of model parameter choice by exploiting variables in Glen's flow law.

2 Derwael Ice Rise

Derwael Ice Rise has a grounded area of roughly 1050 km^2 and is an isle-type ice rise with a ridge divide. The grounded area has a maximum width of roughly 35 km perpendicular to the predominant flow direction of the ice shelf. The ice rise has a maxi-

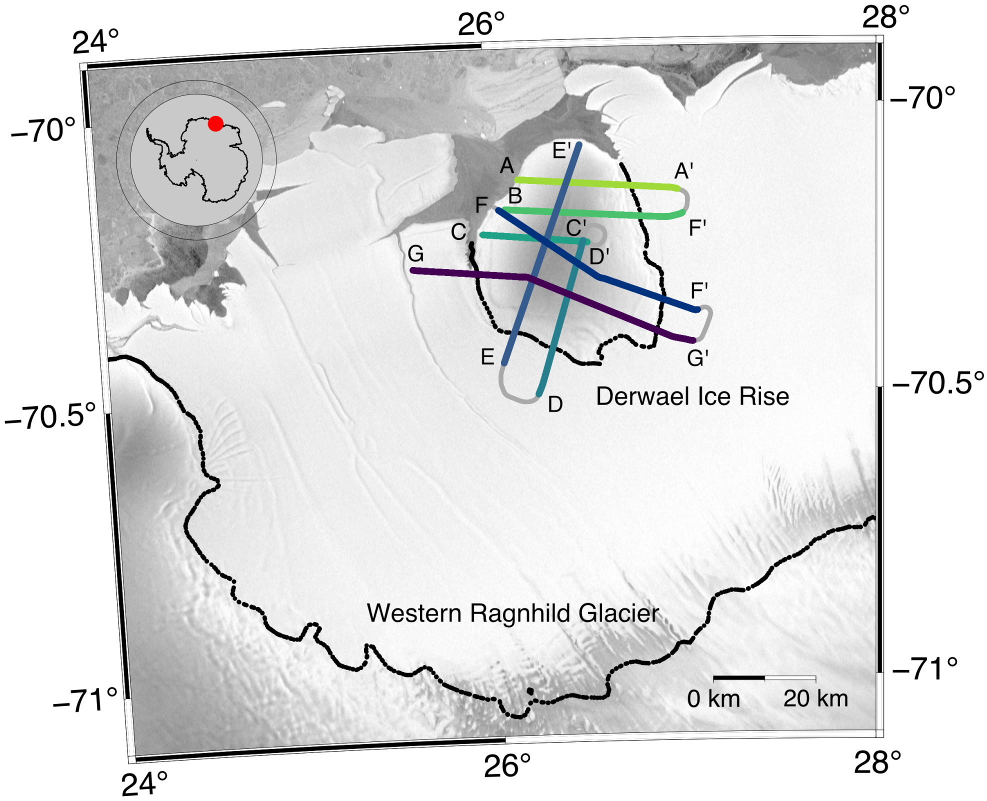

Figure 1. The location of Derwael Ice Rise within the Roi Baudouin Ice Shelf in East Antarctica. The coloured line segments $A - A'$ to $G - G'$ indicate the locations of radar measurements taken using airborne radar. The continental and ice rise grounding lines are indicated by the black lines. The RADARSAT mosaic (Jezek, 2003) is shown in the background, and the grounding line (black dots) is from Morlighem et al. (2020).

mum ice thickness of roughly 630 m with an estimated accuracy of 5 % (Morlighem et al., 2020) and is thickest in the south of the ice rise, where there is convergence of flow from the ice rise and the ice shelf. The maximum ice thickness at the ridge divide is roughly 540. We choose Derwael Ice Rise because of the availability of radar data across the ice rise divide and the shear margins, and also because Derwael Ice Rise is close to steady-state, perhaps with some current thinning (Drews et al., 2015; Callens et al., 2016). Derwael Ice Rise has well expressed isochrone arches beneath the ridge divide. A pecularity is, that arches (referred to as side arches later on) also occur in the south-eastern flanks close to the divide (Drews et al., 2015). An ice rumple is located in the north-western corner of the domain.

3 Methods

The model setup is based on Henry et al. (2022), and here we extend the framework to real-world geometries. In the following sections, we describe the required modifications to accomplish this. We use the finite element software Elmer/Ice (Gagliardini et al., 2013) to solve the Stokes equations. Here, we describe the coupled equations, model parameters boundary conditions and mesh resolution.

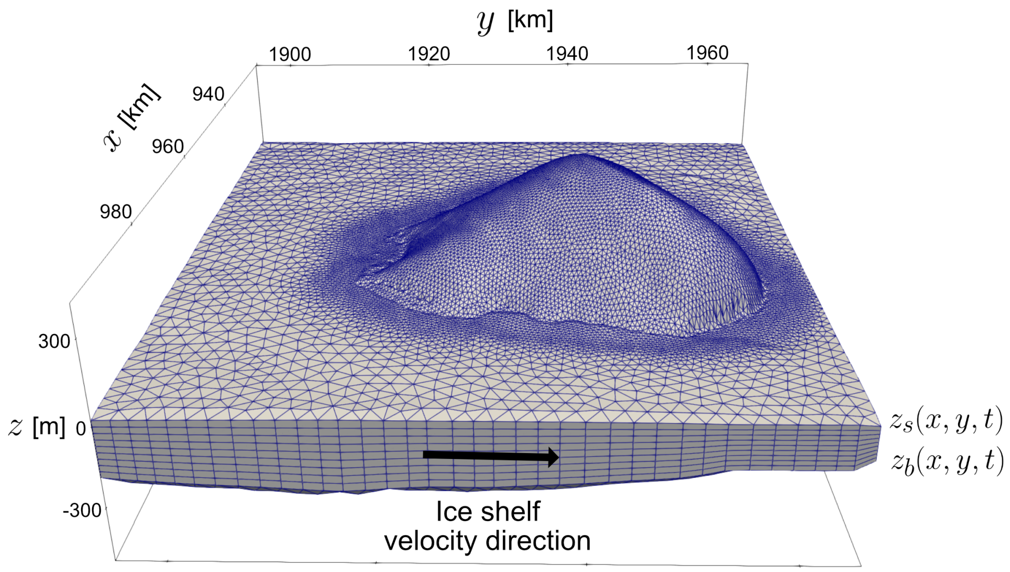

Figure 2. The model set up with horizontal distances in Antarctic polar stereographic projection. The area encompassing the ice rise has a characteristic resolution of 500 m and the surrounding area has a resolution of 2000 m. The upper ice surface is denoted by $z_s = z_s(x, y, t)$ and the lower ice surface by $z_b = z_b(x, y, t)$, where x and y are the horizontal directions and z is the vertical direction relative to sea level. Note: for visualisation, the vertical is scaled by a factor of 30.

Table 1. List of parameters used in the simulations

Parameter	Symbol	Value	Unit
Basal friction exponent	m	1/3	
Local ocean density	ρ_w	1000	kg m^{-3}
Ice density	ρ_i	900	kg m^{-3}
Gravity	g	9.8	m s^{-2}
Universal gas constant	R	8.314	mol^{-1}K^{-1}
Geothermal heat flux	ϕ_q	50	mWm^{-2}
Basal melt parameter	b_0	0.95	ma^{-1}

3.1 Governing equations

The Stokes equations,

$$\boldsymbol{\nabla} \cdot (\boldsymbol{\tau} - P\mathbf{I}) + \rho_i \mathbf{g} = 0, \tag{1}$$

describe the flow of ice, where $\boldsymbol{\tau}$ is the deviatoric stress tensor, P is the pressure, $\mathbf{I}$ is the identity matrix, ρ_i is the ice density and $\mathbf{g} = -g\hat{\mathbf{e}}_z$ is the gravitational acceleration. The ice is subject to an incompressibility condition,

$$\boldsymbol{\nabla} \cdot \mathbf{u} = 0. \tag{2}$$

The Glen's power flow law,

$$\boldsymbol{\tau} = 2\eta\dot{\boldsymbol{\varepsilon}}, \tag{3}$$

describes the nonlinear dependence between the strain rate tensor, $\dot{\boldsymbol{\varepsilon}}$, and the deviatoric stress tensor. The effective viscosity, η, is

$$\eta = \frac{1}{2} A(T)^{-1/n} \dot{\varepsilon}_e^{(1-n)/n}, \tag{4}$$

where $A(T)$ is the ice fluidity which is dependent on temperature, T, and is described in detail below. The effective strain rate, $\dot{\varepsilon}_e^2$, is the square of the second invariant of the strain rate tensor, $\dot{\boldsymbol{\varepsilon}}$. As in Gagliardini et al. (2013), the temperature of the ice evolves subject to

$$\rho_i c_v \left(\frac{\delta T}{\delta t} + \mathbf{u} \cdot \boldsymbol{\nabla} T \right) = \nabla \cdot (\kappa \boldsymbol{\nabla} T) + \mathbf{D} : \boldsymbol{\sigma}, \tag{5}$$

where : is the double inner product,

$$c_v = 146.3 + 7.253T \tag{6}$$

is the specific heat capacity of the ice and

$$\kappa = 9.828 \exp\bigl(-5.7 \times 10^{-03} T\bigr) \tag{7}$$

is the thermal conductivity (Ritz, 1987). The temperature is coupled to the Glen's flow law using an Arrhenius law

$$A(T, p) = EA_0 \exp(-Q/RT), \tag{8}$$

where A_0 is a constant pre-factor, Q is the activation energy and R is the universal gas constant. The Arrhenius law is multiplied by a constant, E, called an enhancement factor, in order to obtain an optimal coefficient in the Arrhenius law. The combination of the parameters A_0 and E are used in ice sheet modelling to account for effects such as grain size, crystal orientation, impurities, porosity and water content. An exploration of the influence of each process is beyond the scope of this study, but we will note here that processes which soften ice cause either an increase in the parameter A_0 or E. For calculating the equivalent Arrhenius factor for a Glen's flow law exponent of $n = 3$, we take a similar approach to Zeitz et al. (2020) and use a first estimate of the stress magnitude of $[\tau_0] = 0.25 \times 10^6$ Pa, so that

$$A_0\big|_{n=4} \exp\bigl(-Q\big|_{n=4}\bigr) = \frac{A_0\big|_{n=3} \exp\bigl(-Q\big|_{n=3}\bigr)}{[\tau_0]}. \tag{9}$$

The first estimate of τ_0 is to compensate for the multiplication of an additional deviatoric stress tensor in Glen's flow law. The upper surface temperature is set equal to the temperature field data (Comiso, 2000). Initially, a linear temperature profile from the lower ice surface to the upper ice surface is prescribed. During transient simulation, the upper and lower surface temperatures evolve subject to a Neumann boundary condition.

During initialisation, the lower ice surface temperature is prescribed to be the pressure melting point temperature,

$$T_p = 273.15 - \beta \rho_i g (z_s - z). \tag{10}$$

Here, β denotes the Clausius-Clapeyron constant, $\beta = 9.8 \times 10^{-8}$ K Pa^{-1} (Zwinger et al., 2007). In order to solve for the isochronal stratigraphy of the ice, the age of the ice is solved according to

$$\frac{\partial \psi}{\partial t} + \mathbf{u} \cdot \nabla(\psi) = 1 \tag{11}$$

where ψ is the age of the ice (Zwinger & Moore, 2009). Eq. 11 is solved using a semi-Lagrangian scheme implemented in Elmer/Ice (Martín & Gudmundsson, 2012).

The upper ice surface, $z = z_s(x, y, t)$, and the lower ice surface, $z = z_b(x, y, t)$, evolve subject to

$$\left(\frac{\partial}{\partial t} + \mathbf{u} \cdot \boldsymbol{\nabla} \right) (z - z_s) = \dot{a}_s, \tag{12}$$

and

$$\left(\frac{\partial}{\partial t} + \mathbf{u} \cdot \boldsymbol{\nabla} \right) (z - z_b) = \dot{a}_b, \tag{13}$$

respectively, where $\dot{a}_s = \dot{a}_s(x, y)$ is the ice-equivalent SMB. The basal melt rate, $\dot{a}_b = \dot{a}_b(x, y)$, is set to a suitable constant of 0.95 m a^{-1} which resulted in minimal adjustment of ice shelf thickness and grounding line position and is close to the average spatial value of 0.8 m a^{-1} across the Roi Baudouin Ice Shelf (Drews et al., 2020). The SMB, $\dot{a}_s$, is described in further detail below. Where ice is in contact with the bed, a non-linear Weertman friction law (Weertman, 1957) is used,

$$\boldsymbol{\tau}_b = -C |\mathbf{u}_b|^{m-1} \boldsymbol{u}_b, \tag{14}$$

where $\boldsymbol{\tau}_b$ is the basal shear stress, C is a constant friction coefficient, $\boldsymbol{u}_b$ is the velocity tangential to the bed, and m is the friction law exponent and has the value $m = 1/3$ in all simulations.

For all our simulations, we use a horizontal resolution of 500 m in the area encompassing the ice rise up to a distance from the grounding line of 5000 m and the surrounding area has a resolution of 2000 m (Fig. 2). In the vertical, the mesh is made up of 10 layers. The higher resolution is needed in order to better resolve the stratigraphy of the ice rise. The Elmer/Ice grounding line implementation *Discontinous* is used.

3.2 Observational data, initial conditions and boundary conditions

3.2.1 Observational stratigraphy

Airborne radar data were acquired in the 2018/19 Antarctic field season as part of the CHIPSM survey using the Polar 6 aircraft of the Alfred Wegener Institute with an ultrawideband radar (MCoRDS v5) and eight-element fuselage antenna array operating in the 150–520 MHz frequency range. Details on data processing and tracing of isochronal internal layers is laid out in (Koch, Drews, Franke, et al., n.d.), which use the same data set. Dating of the two shallowest internal layers along the radar profiles is based on an ice-core depth scale (Philippe et al., 2016) under the assumption of a steady-state age-depth relation (Koch, Drews, Franke, et al., n.d.). This yields a total of seven profiles across the ice rise (Fig. 1).

In order to make comparisons between the modelled isochronal stratigraphy and the observed internal reflection horizons possible, a density adjustment needs to be made. This can be done either by adjusting the modelled isochrone elevation to match the density profile of the real-world ice rise or vice versa. We choose the latter. The adjustment

Table 2. List of simulations

Simulation	n	E	Pre-factor 1 [Pa^{-n} a^{-1}]	Pre-factor 2 [Pa^{-n} a^{-1}]
n3E0.2	3	0.2	1.258×10^7	6.046×10^{22}
n3E0.4	3	0.4	1.258×10^7	6.046×10^{22}
n3E0.5	3	0.5	1.258×10^7	6.046×10^{22}
n3E0.6	3	0.6	1.258×10^7	6.046×10^{22}
n3E0.8	3	0.8	1.258×10^7	6.046×10^{22}
n3E1.0	3	1.0	1.258×10^7	6.046×10^{22}
n4E1.2	4	1.2	5.032×10^7	2.419×10^{23}
n4E1.6	4	1.6	5.032×10^7	2.419×10^{23}
n4E1.8	4	1.8	5.032×10^7	2.419×10^{23}
n4E2.0	4	2.0	5.032×10^7	2.419×10^{23}
n4E2.4	4	2.4	5.032×10^7	2.419×10^{23}
n4E2.8	4	2.8	5.032×10^7	2.419×10^{23}

results in isochrone elevations equivalent to a constant density of 900 kg m^{-3} and is calculated according to the density profile of Derwael Ice Rise in Callens et al. (2014). Throughout the paper, when referring to depth below surface in relation to observations, these are relative to the BedMachine surface elevation, adjusted to an equivalent of 900 kg m^{-3} as opposed to the 917 kg m^{-3} assumed in BedMachine. On the other hand, when referring to depth below surface in relation to model results, depths are relative to the steady-state modelled surface using a denisty of 900 kg m^{-3}. Note that this choice does not have an effect on the final comparison between the modelled and observed isochrones.

3.2.2 Surface and basal mass balances, velocity, bed and ice geometry

Over the ice rise, we derive the SMB along transects from the shallow radar stratigraphy using the standard approach of the shallow layer approximation (Waddington et al., 2007). Isochrones are dated using an ice core drilled at the summit (Philippe et al., 2016). Details of this are presented in (Koch, Drews, Franke, et al., n.d.) accompanied by the dataset (Koch, Drews, Muhle, et al., n.d.). We interpolated between radar transects using an interpolation scheme and merge the SMB field at the ice-rise edges with reanalysis data from RACMO2.3p1 mean annual SMB from the years 1979-2014 (van den Broeke, 2019). Including the SMB estimates from radar observations is a critical step in the analysis because the reanalysis data are too coarsely resolved on the ice rise. In order to avoid model drift due to uncorrected offsets in the SMB field, we correct the SMB field by subtracting it by the rate of change of the surface elevation after 50 years of simulation time.

At the domain boundary on the oceanward side of the ice rise, the ice is allowed to flow subject to hydrostatic pressure. At all other boundaries, depth-independent fluxes are prescribed and are derived from observed velocities (Rignot & Scheuchl., 2017). The bed elevation and the initial ice geometry is prescribed using BedMachine Antarctica data (Morlighem et al., 2020). When comparing BedMachine bed elevation with observations from our radar survey, we found significant mismatches of roughly 150 m in the north-eastern corner of Derwael Ice Rise (Fig. 4). This is surprising given that the radar survey is part of the BedMachine dataset. We see some interpolation artefacts where the grounded ice bed elevation dataset is merged with the bed elevation data below floating ice.

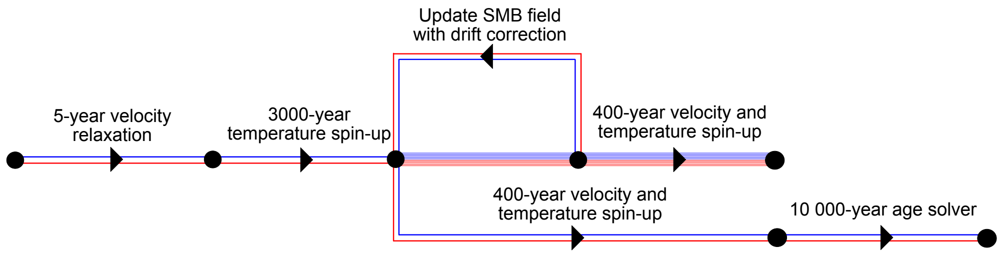

Figure 3. The schematic shows the spin-up procedure for the simulations in Table 2. The blue lines refer to the $n = 3$ simulations and the red lines refer to the $n = 4$ simulations. The black dots indicate the points when the simulation was restarted with a change in model set up as indicated by the schematic labels. Further details regarding the sequence of steps are given in Section 3.3.

3.3 Model spin-up procedure

In order to model the three-dimensional isochronal stratigraphy of an ice rise, the following steps are taken to spin-up the model. The details are as follows and can be seen in Fig. 3.

- Step 1: Simulate the ice rise for 5 years with the Stokes, temperature, and upper and lower free surface solvers on for Glen's flow law exponents of $n = 3$ and $n = 4$.
- Step 2: Spin up the temperature for 3000 years with the Stokes and free surface solvers off.
- Step 3: Simulate with the chosen set of parameters (Table 2) for 400 years.
- Step 4: Choose the optimal $n = 3$ and $n = 4$ simulation based on the least volume change (Fig. 6).
- Step 5: Compute SMB from model drift after allowing the surface elevation to evolve for 50 years. The SMB is adjusted using the model drift over the grounded area and is incorporated with the combined stratigraphy-derived and RACMO2.3p1 SMB field. A Gaussian filter is applied to remove steep gradients.
- Step 6: Simulate with the temperature, free surface and Stokes solvers activated for 400 years.
- Step 7: Run the age solver with the Stokes, free surface and temperature solvers off for 10000 years.

4 Results

4.1 Model parameter choice and applied surface mass balance

In contrast to the SMB field from the RACMO2.3p1 simulation, the highest values of the stratigraphy-derived and drift-corrected SMB are concentrated in the centre of the ice rise (Fig. 5 in the Supporting Information). Here, the differences in spatial variation before and after the drift correction are evident, with the drift-corrected SMB being concentrated more towards the west of the ice rise. RACMO2.3p1 data shows higher values on the eastern and northern sides of the ice rise, whereas the stratigraphy-derived and drift-corrected SMB has higher values in the centre and on the south-western side of the ice rise. The results are close to mean SMB values of 0.47 ± 0.02 m w.e. a^{-1} (for comparison with our results, this is equivalent to 0.52 ± 0.02 m a^{-1} assuming an ice density of 900 kg m^{-3}) for the period 1816−2011 found by (Philippe et al., 2016), derived from an ice core at the summit of Derwael Ice Rise.

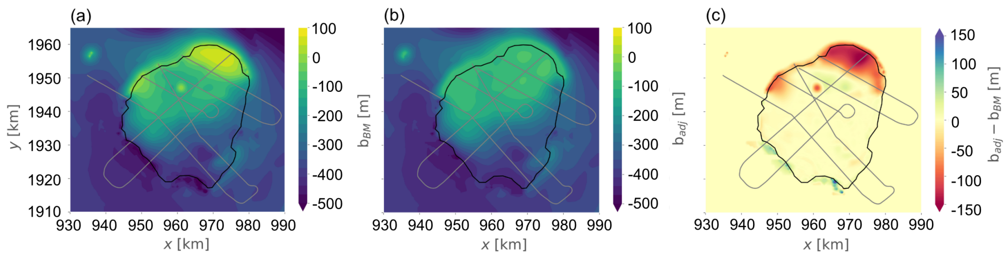

Figure 4. The BedMachine Antarctica bed elevation is shown in (a) and the adjusted bed elevation after re-interpolation and smoothing of unphysical anomalies is shown in (b). The difference between the adjusted bed elevation and the original BedMachine bed elevation is shown in (c). The grey lines show the location of radargrams with which the simulations are compared. The bed elevation data from these radar lines has been used in the BedMachine data.

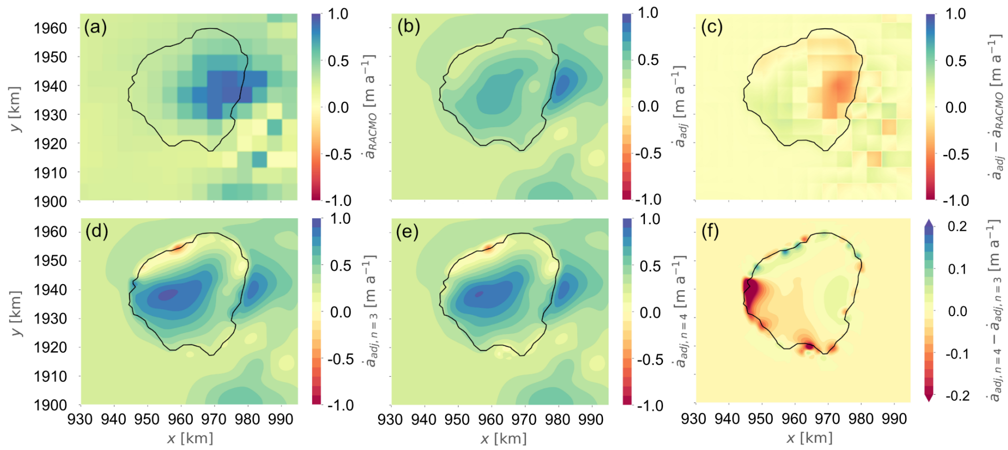

Figure 5. Surface mass balance (SMB) (a) based on RACMO2.3p1 data; (b) the adjusted product from a combination of stratigraphy-derived data in the grounded area and RACMO2.3p1 data in the surrounding area; (c) difference between the adjusted and the RACMO2.3p1 SMB. The SMB in (d) and (e) use a drift correction made with the $\partial z_s/\partial t$ field after a simulation time of 50 years for the $n = 3$ and the $n = 4$ simulations, respectively and (f) shows the difference in SMB between the $n = 3$ and $n = 4$ simulations for the stratigraphy-derived and drift-corrected SMB.

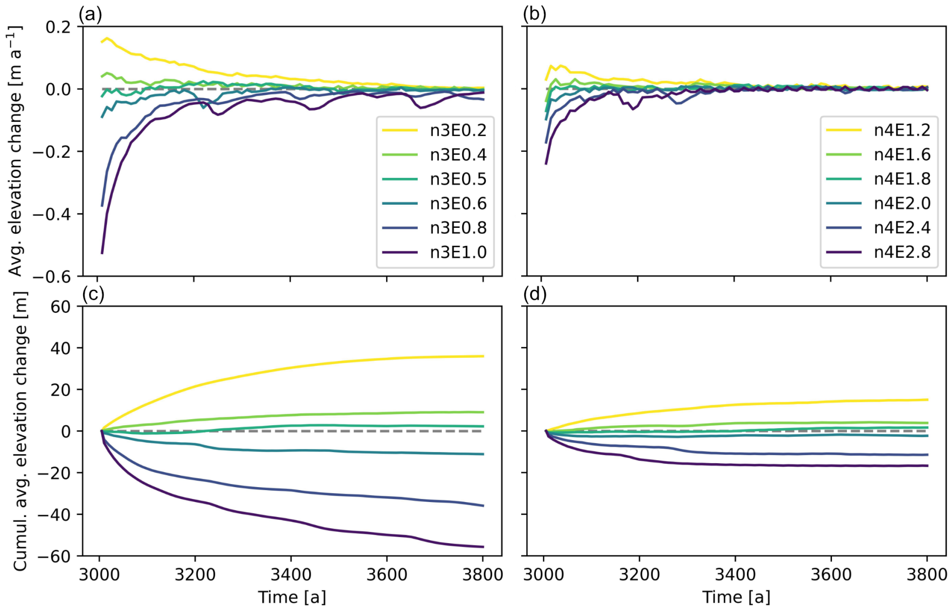

Figure 6. Elevation changes for different simulations: (a) and (b) show the average elevation changes, and (c) and (d) show the cumulative elevation changes for Glen's flow law exponents of $n = 3$ and $n = 4$, respectively, for varying enhancement factors. Legends indicate the different model runs in colour.

In order to find the optimal combination of parameters in the simulations of Derwael Ice Rise, an ensemble of simulations for various enhancement factors were performed. Here we note that in this work we take the enhancement factor to simply be a constant multiplier that adjusts the Arrhenius factor, A_0 and is equivalent to adjusting the Arrhenius pre-factor itself. As a performance evaluation metric in order to find the optimal enhancement factor, we use the change in surface elevation with respect to time across the grounded ice (Fig. 6), assuming that Derwael Ice Rise is in steady state. We found that an enhancement factor of $E = 0.5$ (simulation $n3E0.5$) produced an ice rise with the least cumulative volume change in the $n = 3$ simulations. For the $n = 4$ simulations, a corresponding enhancement factor of $E = 1.8$ (simulation $n4E1.8$) is found. Henceforth, we refer to the $n3E0.5$ and the $n4E1.8$ simulations simply as the $n = 3$ and $n = 4$ simulations, respectively. Large fluctuations seen in Fig. 6 (c) and (d) are due to sudden changes in grounding line position and temporary localised decreases in elevation. Simulations with an underestimated or overestimated enhancement factor result in elevation and volumetric changes.

In both the $n = 3$ and the $n = 4$ simulation, there is a slight reduction in ice thickness at the divide compared with the BedMachine data of roughly 15 m (corresponding to 3 % of the ice thickness at the divide). This reduction in ice thickness is less in the $n = 4$ than the $n = 3$ simulation. On the western side of the ice rise excess thinning of the ice occurs, whereas in all other grounding zones, too much thickening occurs. Comparing the elevation change between the $n = 3$ and $n = 4$ simulations (Fig. 8), it can be seen that the steady-state $n = 3$ simulation has a lower elevation in the centre of the ice rise than the $n = 4$ simulation. In the north-eastern flank of the ice rise, the $n = 3$ simulation has a lower steady-state surface elevation than the $n = 4$ simulation, but all other flanks show a tendency for a higher surface elevation in the case of the $n = 3$ simulation.

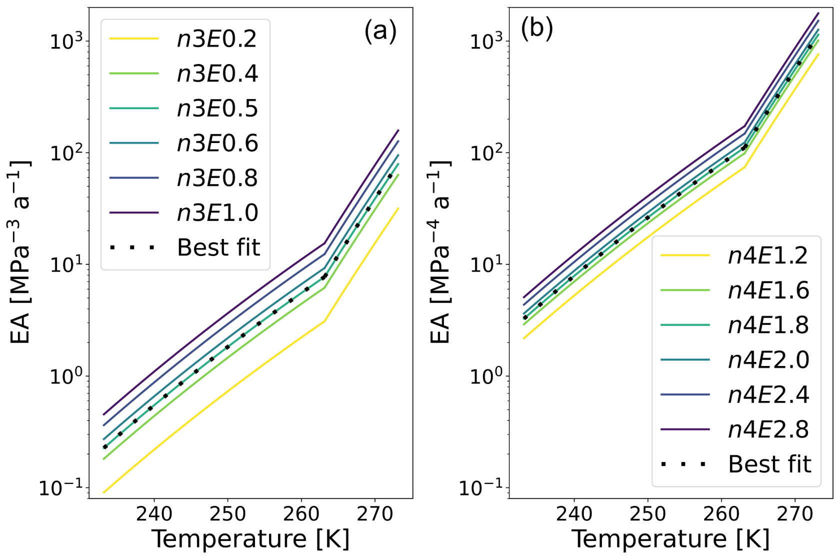

Figure 7. The relationship between the temperature and the Arrhenius law multiplied by varying enhancement factors, E; (a) corresponds with the $n = 3$ simulations and (b) with the $n = 4$ simulations. Note the y-axes have a logarithmic scale. In (a) and (b), the dotted lines indicate the most suitable combination of parameters for the simulations of Derwael Ice Rise.

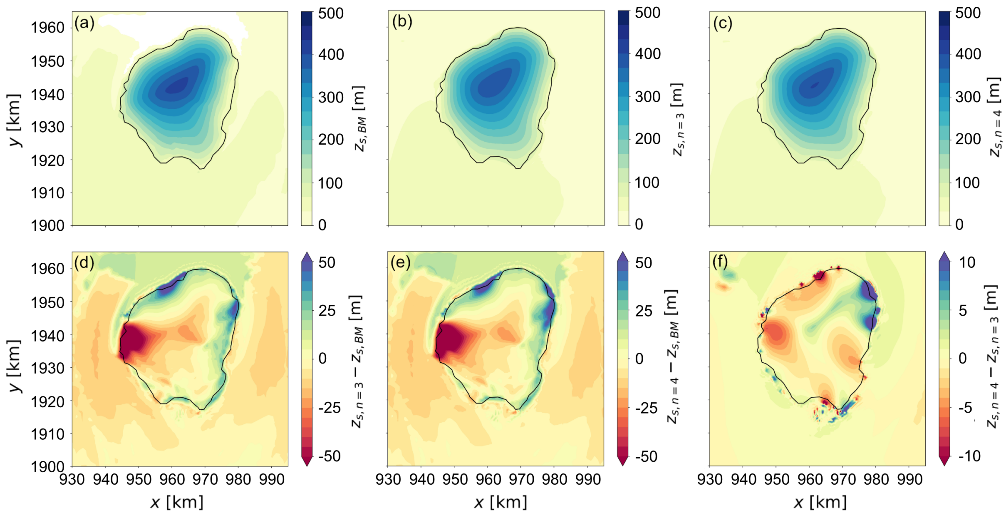

Figure 8. Surface elevation (a) from BedMachine Antarctica data, and (b) and (c) show the surface elevation of the $n = 3$ and $n = 4$ simulations, respectively, after the 400 year transient velocity spin up. The difference in surface elevation between the $n = 3$ simulation and the BedMachine data is shown in (d), the difference in surface elevation between the $n = 4$ simulation and the BedMachine data is shown in (e) and the difference in surface elevation between the $n = 4$ simulation and the $n = 3$ simulation is shown in (f). Note that (f) has a different colour scale than (d) and (e).

4.2 Comparisons between modelled and observed stratigraphy

Our new modelling framework allows us to further understand the similarities and differences between the observational data of Derwael Ice Rise and the simulated ice rise. Modelled isochrones are compared with dated isochrones derived from the radargrams obtained using airborne radar measurements. The radar measurements cover areas of Derwael Ice Rise including the ridge divide, flanks and grounding zones. The data is divided into seven cross-sections, each of which is compared with the model output for both $n = 3$ and $n = 4$ (Fig. 9). The modelled isochrones broadly reproduce the observed isochrones. The largest discrepancies between modelled and observed stratigraphy correspond to regions of the domain where the modelled and observed surface geometry do not match. For example, due to the tendency of the ice rise to broaden and thicken at the grounding zones and decrease in elevation in the centre during transient evolution, the elevation of the isochrones in these regions is generally under-estimated in the centre of the ice rise and over-estimated in the grounding zones. Evidence for this is provided by the cross-section $A{-}A'$ (Fig. 9a). There is a significant mismatch of up to 50 m between the modelled and observed isochrones, particularly on the eastern side which is likely due to an incorrect bed elevation. Mismatches with similar characteristics are also present in cross-sections $B - B'$, $C - C'$ and $F - F'$.

Fig. 10 shows the difference between the observed and modelled $n = 3$ isochronal slope for the cross-sections $A{-}A'$ to $F{-}F'$ in Fig. 1. Generally, the slopes of the modelled isochrones match well with the observed isochronal slopes. Areas where there is a close match between observed and modelled isochrones are indicated by white in Fig. 10. At all grounding lines around the ice rise, there is significant steepening of isochrones due to the downward motion of ice. Given the general tendency of the ice rise to broaden in the grounding zones, the steepening of the modelled isochrones tend to be located a small distance from the observed isochrones, but reproduce similar patterns in isochrone geometry. On the stoss side of the ice rise, thinning of the stratigraphy indicates sudden acceleration of ice a few kilometres away from the grounding line. This is particularly evident in the cross-sections $A - A'$.

In the observational data, the Raymond arch at the ridge divide is visible in the cross-sections $B{-}B'$, $C{-}C'$, $F{-}F'$ and $G{-}G'$. The side arch identified in Drews et al. (2015) is also visible in the cross-section $F{-}F'$. In Fig. 9e, the side arch visible in the observed isochrones is noticeable at a depth corresponding to the first modelled isochrone below the surface, which has an age of 100 years.

4.3 Velocities and strain rates

Simulated ice-shelf velocities on the western side of the ice rise are over 300 ma^{-1} and roughly 200 ma^{-1} on the eastern side. This is because of the location of the tributary Western Ragnhild Glacier. The asymmetry of the surrounding ice shelf results in an asymmetry in the divergence of the flow of ice around the ice rise. The simulated velocity field of the ice rise shows a distinct ridge divide on the northern side of the ice rise, with the divide positioned diagonally from the north east to the south west.

Absolute surface velocity differences between the $n = 3$ and the $n = 4$ simulations are generally below 10 % with the exception of the divide and the north-eastern and south-eastern sides of the ice rise (Fig. **??** in the Supporting Information). The largest negative velocity differences occur in north-eastern and south-eastern sides of the ice rise with higher velocities in the $n = 3$ simulation. In the talwegs, velocities are higher in the $n = 4$ simulation. Note that talweg is a term first introduced in relation to ice rises in Gillet-Chaulet et al. (2011) and is a geomorphological term describing a valley. At the ridge divide, the velocities are significantly lower in the $n = 4$ simulation than the $n = 3$ simulation. In the areas perpendicular to the centre of the ridge divide, the $n = 4$ simulation has higher velocities than the $n = 3$ simulation. Elsewhere, the $n = 3$ sim-

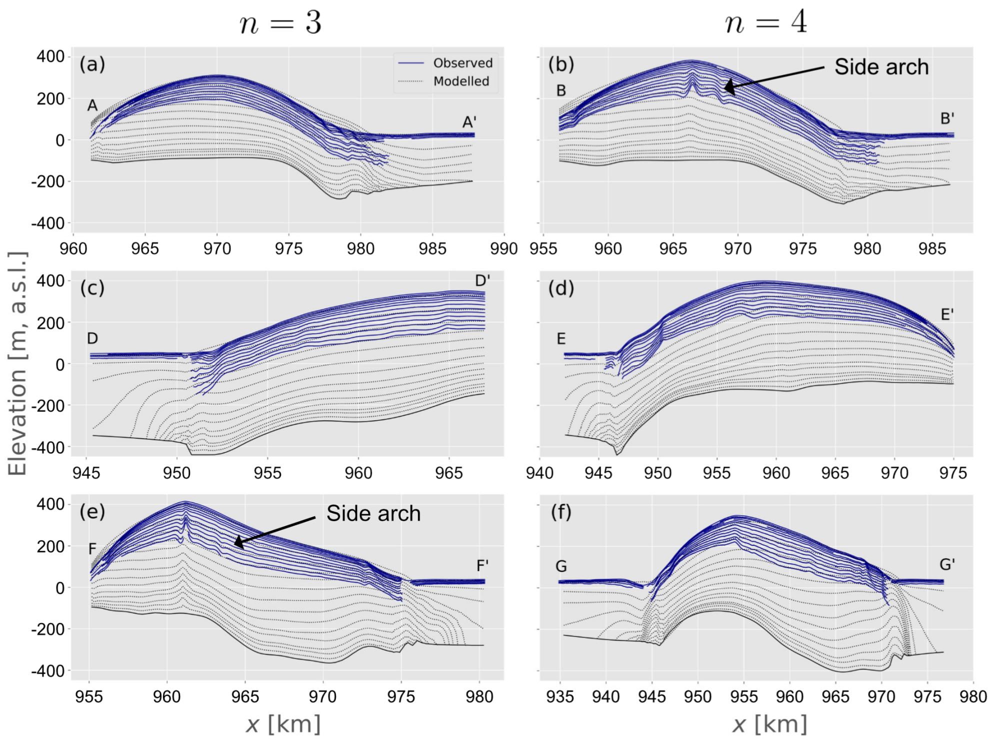

Figure 9. Comparisons between modelled and observed stratigraphy along radar profiles marked in 1 in the vertical domain of the model. Graphs in left columns, (a), (c), and (e), show comparisons for a Glen's flow law exponent of $n = 3$ (cross-sections $A - A'$, $D - D'$ and $F - F'$), and the right column, (b), (d), and (f), show comparisons for a Glen's flow law exponent of $n = 4$ (cross-sections $B - B'$, $E - E'$ and $G - G'$). The blue solid lines show the observed stratigraphy and the dotted black lines show the modelled stratigraphy.

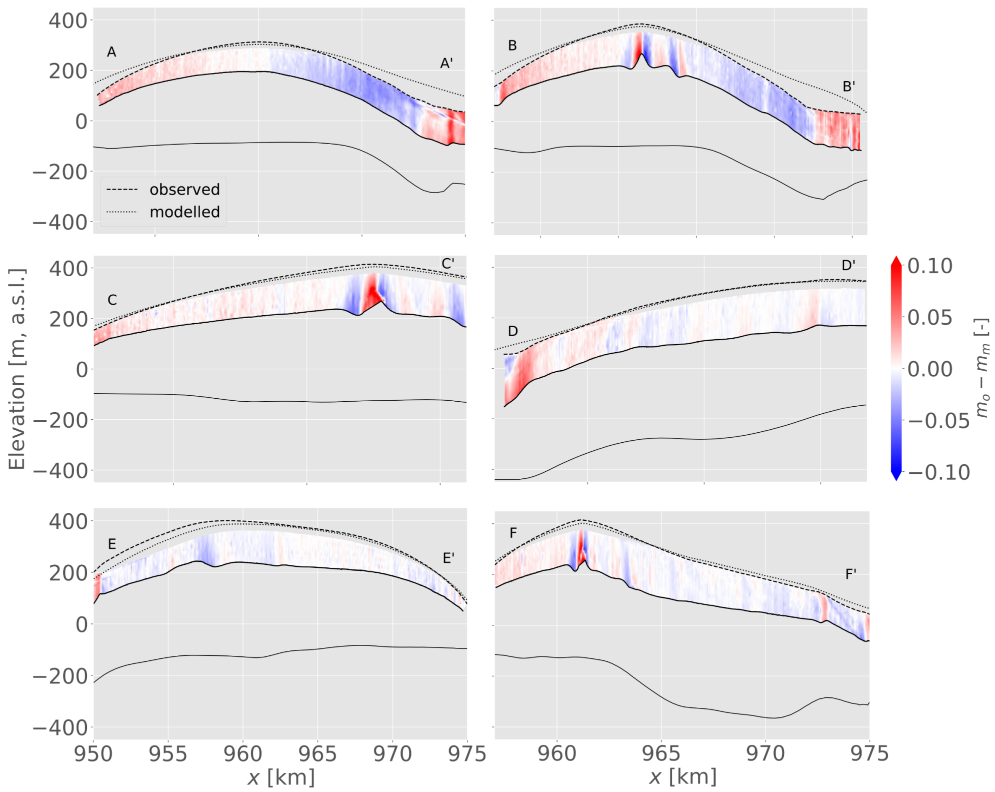

Figure 10. Difference between observed isochrone slope (m_o) and the $n = 3$ modelled isochrone slope (m_m) at locations where data is available for both. The cross-sections $A - A'$ to $F - F'$ correspond with the radar profiles in Fig. 1. The dashed lines show the observed ice surface and the dotted lines show the modelled surface. The lower extent of the area of comparison and the lower ice surface are shown with solid black lines.

ulation has higher velocities than the $n = 4$ simulation. A similar pattern of velocity difference between the $n = 3$ and the $n = 4$ simulations is observed at the depth of the 1000 year isochrone (Fig. **??** in the Supporting Information). Percentage differences in velocities are more pronounced in the talwegs at the 1000 year isochrone than at the ice surface. The flanks perpendicular to the ridge divide show higher velocities in the case of the $n = 4$ simulation than the $n = 3$ simulation. Furthermore, there are pronounced higher velocities in the $n = 3$ simulation in the south of the ice rise. Here, there is higher divergence of the velocity vectors (Fig. 12a), but not enough for an additional ridge or Raymond arches to form.

At the base of the ice rise, some basal sliding occurs. Lowest basal velocities of $<$ 1 ma^{-1} are simulated under the ridge divide and increase towards the flanks of the ice rise (Fig. **??**a in the Supporting Information). Interestingly, from the centre of the ice rise to the south-eastern corner, there is an area of low velocity compared with elsewhere in the flanks of the ice rise. In three locations in the grounded ice, close to the grounding line, there is a higher basal sliding velocity of 5 ma^{-1}. This indicates that there is a higher effective stress in these areas, leading to acceleration of the ice. In both the $n = 3$ and $n = 4$ simulations, the same basal friction parameterisation is used, and so differences in the basal velocities are due to feedbacks with the overlying ice. A comparison of the basal velocities between the two simulations reveals that the largest differences are seen in the grounding zones, where basal velocities in the $n = 4$ simulation are higher than in the $n = 3$ simulation (Fig. **??**b in the Supporting Information). In the interior of the ice rise at the flanks of the ridge divide, velocities in the $n = 3$ simulation are higher than in the $n = 4$ simulation.

The computed ice surface shear strain rate in the direction of ice flow shows a similar pattern to the ice velocity. Higher shear strain rates are observed on the western side of the ice rise. These result from the larger velocities in the ice shelf (Fig. 11). On the eastern side of the ice rise, the shear strain rates are lower than on the western side. The areas of higher shear strain rate on the eastern side are concentrated in two areas; in the north east and the south east of the ice rise. The area of lower shear strain rate between the areas of higher shear strain rate are a consequence of velocities from the ice rise and ice shelf being more similar in magnitude. Differences in shear strain rates between the $n = 3$ and $n = 4$ simulations primarily occur on the western side of the ice rise. Differences on the eastern side of the ice rise are negligible in comparison and localised differences are likely due to slight differences in grounding line position.

Differences in ice velocity between the simulations also affect the computed internal stratigraphy. For both simulations, the oldest ice at a depth of 95 % is located at the ridge and on the stoss side of the ice rise. Here, convergence of flow from the ice rise and the ice shelf results in relatively stagnant ice velocities (Fig. **??** in the Supporting Information). The age field at a depth of 95 % shows that ice is on average 335 years older in the case of the $n = 3$ simulation. This reflects the higher strain rates and thus enhanced thinning of ice under a higher Glen's flow law exponent. At a depth of 50 %, differences in age are much less, with ice being between 25 and 50 years older at the divide in the case of the $n = 4$ simulation. The largest differences in age at a depth of 50 % are seen in the area of compression between the ice rise and the ice shelf and in the north-eastern corner of the ice rise, with ice being more than 50 years older in the case of the $n = 4$ simulation. The opposite is seen in the talwegs, where ice is older in the case of the $n = 3$ simulation at a depth of 50 %.

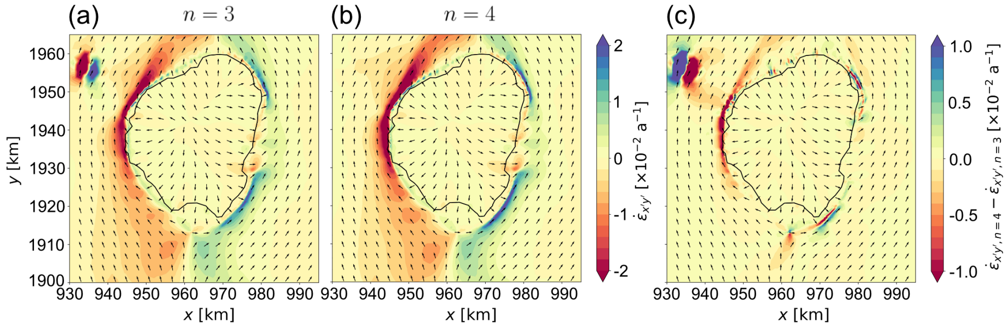

Figure 11. Shown in (a) and (b) is the shear strain rate for the $n = 3$ and $n = 4$ simulations, respectively, calculated by rotating the strain rate tensor to align with the velocity direction. In (c), the difference between the shear strain rate in the direction of the velocity of the $n = 4$ and $n = 3$ simulations is shown.

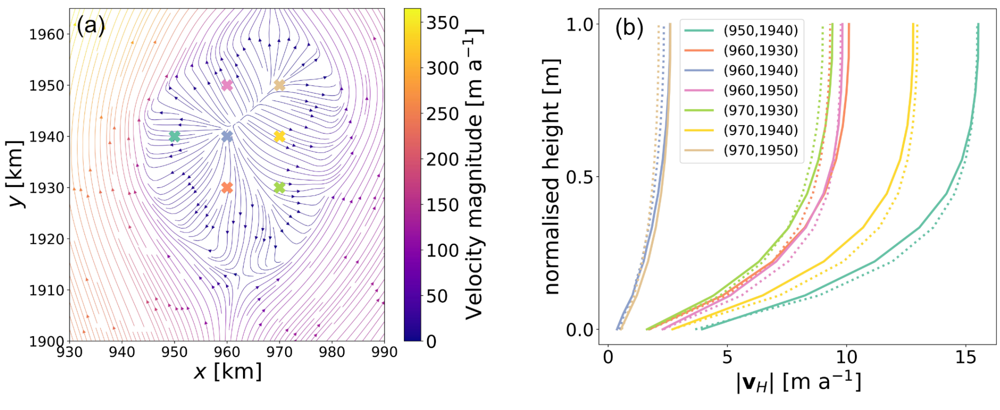

Figure 12. (a) shows the velocity field of Derwael Ice Rise, (b) shows the horizontal velocity magnitude for the (x, y) coordinates marked in (a), for the $n = 3$ simulation (solid lines) and the $n = 4$ simulation (dashed lines).

5 Discussion

5.1 Progress and challenges for three-dimensional ice rise modelling

Previous research has highlighted the importance of ice rises in deciphering past re-organisation of flow. Until now, the comparison between observed and modelled internal stratigraphy has been restricted to flow-line setups, providing a spatially limited assessment (Martín et al., 2006, 2009; Drews et al., 2015). We introduce a new three-dimensional modelling framework that overcomes these limitations and allows us to provide a spatially continuous age field that can be compared with radar observations. This provides an important step towards the routine simulation of ice rises and the ultimate goal of using them to constrain paleo ice-sheet simulations.

During the development of our modelling framework, we encountered a number of challenges. Given their small size, ice rises are often insufficiently resolved in continental-scale boundary datasets such as BedMachine or RACMO2.3p1. This can only be overcome if in-situ and high-resolution datasets are available to correct for these mismatches. The multiple steps necessary to spin-up the model are in parts subjective and a different sequence of spin-up steps of different simulation lengths may result in slightly differing results. As highlighted previously, it is important to note that interpolation errors in the bed elevation do occur and it may be necessary to make comparisons with the raw data. Failure to correct anomalies in the bed elevation data can result in artefacts in transient simulations, for example, a thickening of the ice rise after initialisation. This highlights the importance of such measurements to allow such studies for other ice rises around Antarctica.

The drift correction to the SMB implemented in our study results in an SMB field which is higher than the RACMO2.3p1 dataset (roughly 0.5 m a^{-1} higher) in the centre of the ice rise and lower closer to the margins of the ice rise than in the stratigraphy-adjusted SMB field. This points to a slight over-compensation of the ice softness and perhaps missing processes at the margins of the ice rise such as fracturing, higher melt rates or an anisotropic fabric or another process which would increase the velocity of the ice in that area. Another explanation is that the ice in the centre of the ice rise is stiffer in reality than in the model. As shown in Martín et al. (2009) and Martín and Gudmundsson (2012), anisotropic evolution of ice is a mechanism which enhances the stiffness of ice at an ice divide and the lack of this mechanism in our model is a likely reason for excess thinning of ice at the divide.

5.2 Comparison between modelled and observed stratigraphy

Much progress has been made in comparing modelled and observed internal stratigraphy (Sutter et al. (2021) and Born and Robinson (2021)) on large scales. For Stokes simulations, comparisons between modelled and observed stratigraphy have only been performed for two-dimensional simulations (Martín et al., 2009; Martín & Gudmundsson, 2012; Drews et al., 2015) and have so far not included the grounding line and the surrounding shelf. Including the ice shelf in the simulation domain means that grounding zone processes are included in the simulations and the domain boundaries are no longer within the bounds of the grounded area of the ice rise. Such a setup also allows investigation of isochrones in the shear zone between the ice rise and ice shelf which is characterised by steep isochrone geometries that are difficult to capture with radar observations.

The comparisons between the observed and modelled isochronal slopes in Fig. 10 show a close fit overall, with larger differences in the north east of the ice rise where issues with the bed elevation were found. Furthermore, differences are larger at the main Raymond arch where too coarse vertical resolution results in greater mismatches. Differences in isochrone slopes are primarily due to a mismatch in the surface elevation between modelled and observed results. The largest differences are seen in the north east of the ice rise and at the main Raymond arch and the side arch, which is not captured in the model. The side arch visible in the observed isochrones in Fig. 9e is visible at a depth corresponding to the first modelled isochrone below the surface which has an age of 100 years.

By studying areas where the surface elevation between the observed and modelled stratigraphy is similar, we can identify processes in ice dynamics which are not reproduced by the model. In cross-section $D{-}D'$, there is a deviation in isochrone slope at $x = 957$ km when comparing the modelled isochrones to the observed isochrones. A greater thinning of the isochrones in the observed stratigraphy indicates that the modelled ice may not adequately reproduce speed-up of the ice in this area. In the cross-section $G - G'$, the acceleration of ice seen in the observed stratigraphy is not reproduced to the same extent in the model on the western side of the cross-section. On the eastern side of the $G{-}G'$ cross-section, the modelled stratigraphy shows more gentle slopes than the observed stratigraphy, indicating that in the direction of the grounding zone, modelled ice is accelerating more than the observed ice.

The side arch marked in Fig. 9b was discussed in previous work and it was suggested that it may be a result of unresolved three-dimensional effects (Drews et al., 2015). The lack of a side arch in our three-dimensional simulations indicates that this is not the case and we instead hypothesise that Derwael Ice Rise was previously a triple junction ice rise and that a ridge was previously located where the side arch is seen in the observed stratigraphy. If this is the case, then a transition from a triple junction ice rise to a ridge divide ice rise is quite recent (¡ 100 years) as the side arches are also evident close to the surface. This then suggests that ice rises can have signatures of both ice-divide stability (evidenced by the oversized Raymond arches beneath the contemporary divide) and instability (evidenced by the side arch interpreted as a remnant of a ice-divide triple junction). Furthermore, it cannot be ruled out that the flow divide had switched more than once between the main arch and the side arch.

Comparing the modelled isochrones to the observed isochrones in the shear zone, we see that in the grounding zone, the observed isochrones steepen closer to the ice rise interior than the modelled isochrones. This is due to a grounding line advance in the simulations as a result of too little shear softening in the modelled shear zones around the ice rise, perhaps due to missing processes such as fracturing or an anisotropic fabric. An alternative approach to reducing the grounding line advance would be to alter the Arrhenius pre-factor to allow for softer ice, but this would result in a reduction of the ice rise elevation.

5.3 Glen's flow law exponent

In our study, we have investigated the influence of using a Glen's flow law exponent of $n = 3$ and $n = 4$. The $n = 4$ simulation results in a more peaked shape (Fig. 8). Both the $n = 3$ and the $n = 4$ simulations result in a slight lowering of the surface elevation in the ridge divide area, with the $n = 4$ simulation resulting in a surface elevation closer to that of the observed surface elevation. This is an indicator that a Glen's flow law exponent of $n = 4$ is more suitable, but a general tendency for excess thickening in the grounding zones means this result is not without uncertainty. The lower velocities in the $n = 4$ simulation compared with the $n = 3$ simulation align with our understanding of the Raymond effect, with lower velocities and greater Raymond arch amplitude associated with a higher Glen's flow law exponent. Interestingly, the differences in the flanks of the ice rise indicate different responses to the non-linearity that result in slight differences in flow regime.

Predicted age–depth relationships differ by < 5 % in most areas for simulations with $n = 3$ and $n = 4$ (Fig. **??** in the Supporting Information). This suggests that tuning of the Arrhenius factor and the drift-correction for the $n = 3$ and $n = 4$ simulations lead to similar velocity fields in both cases. Exceptions are the divide regions and the shear zones at the ice-rise boundaries where differences are significant. Larger differences are seen in areas where stresses are significantly higher or lower than average stresses. Strain rates in the ice are higher in the $n = 4$ than the $n = 3$ simulation in the shear zones and near the ice-bed interface. Despite these differences, the modelled stratigraphy does not differ significantly. Studies for which an appropriate Arrhenius factor for an exponent of $n = 4$ have so far only been performed with two-dimensional simulations (Martín et al., 2006; Drews et al., 2015), resulting in uncertainties due to the lack of through-plane velocities. A conversion of the Glen's flow law from an exponent of $n = 3$ to $n = 4$ is further complicated by the dependence of the Arrhenius law on the temperature, activation energy, and n itself. Notably, significant uncertainty exists within these parameters as they have been calibrated through few laboratory studies in specific conditions (Zeitz et al., 2020). In our conversion, we neglect differences in activation energies and use a typical stress, $[\tau_0]$, to calculate an initial guess for an appropriate Arrhenius Law for $n = 4$. This simplified scaling is useful as we are able to compare parameters within our model to observed stratigraphy, highlighting the most appropriate values for the flow law. The chosen typical stress is within a reasonable range as in Goldsby and Kohlstedt (2001) and Goldsby (2006). In conjunction with known uncertainties in our understanding of the kinetics of glacier ice, implies that constraints on mechanisms such as temperature, activation energy, and grain size implicit within the Arrhenius relation are necessary to better understand the kinetics of creep on natural glacier ice.

Due to the assumption that ice is incompressible, the horizontal dilation (Fig. **??** in the Supporting Information) is the equivalent of the vertical strain rate, $\dot{\varepsilon}_{zz}$, with a sign change. We assume that differences in strain rate with and without a firn column do not differ greatly. The higher horizontal dilation in the north-western and eastern talwegs in the $n = 4$ simulation than the $n = 3$ simulation implies that there is greater stretching occurring in the ice. The opposite effect is seen in the vicinity of the ice rise ridge divide, with a lower dilation in the case of the $n = 4$ simulation. These small-scale results, which are in agreement with those presented in Gillet-Chaulet et al. (2011), are an analogy for larger scale situations. On larger scales, the higher dilation in areas of high velocity is likely to have consequences for the timing of the onset of an ice stream. Interestingly, in our simulations of Derwael Ice Rise, the south-western region of the ice rise shows a large area where the dilation is lower in the case of the $n = 4$ simulation than the $n = 3$ simulation, resulting in a region which does not contain a ridge divide, but also does not have strain rate differences which one would expect in the talweg of an ice rise. These characteristics are indicative of an ice rise which is in a state close to having a triple junction flow regime. Furthermore, the spatial variation in dilation and the resulting change in distance between isochrones could help in future to determine a correct Glen's flow law exponent.

In Fig. 11, it can be seen that there are higher shear strain rates in the direction of flow in the shear margins in the case of the $n = 4$ simulation than in the $n = 3$ simulation. This result implies softer ice in shear margins when using a $n = 4$ simulation, indicative of viscous deformation at the higher strain rates. When investigating threshold shear strain rates or shear stresses beyond which fracturing occurs, it is important to bear in mind that a differing Glen's flow law exponent will have a differing effect in simulations. An important observation is that the ice rumple north-west of Derwael Ice Rise becomes less grounded in the case of the $n = 4$ simulation, which we attribute to the greater strain-rate softening of the ice for the higher Glen's flow law exponent. This has consequences for simulations including pinning points as the choice of Glen's flow law exponent may have an influence on the buttressing due to that pinning point. Moreover, the higher flux of ice into the ice shelf coming from the talweg on the eastern side of Derwael Ice Rise, results in low shear strain rates in the grounding zone compared with the shear zones upstream and downstream.

5.4 Model limitations and future research directions

We have assumed that Derwael Ice Rise is in steady state and have found parameter values which result in a steady-state geometry close to the present-day observed geometry. Extra care would need to be taken when modelling other ice rises which do not satisfy the steady-state criterion. The boundary and initial conditions of our model are dependent on both observational data and model output (from regional atmospheric climate model RACMO2.3p1). It is important to check for interpolation errors using the raw data. Failure to correct for the bed elevation led to a series of flawed transient simulations in our case. Furthermore, we have not coupled anisotropy evolution to our model as there is insufficient anisotropy data available to constrain the model. Inclusion of ice-anisotropy will increase Raymond arch amplitudes. In future work, three-dimensional ice rises will provide ideal locations for the analysis of differing anisotropy schemes as well as other physical processes such as ice fracture in the shear margins.

Ice rises are good locations to study the effect of ice flow parameters across different flow regimes. The isochronal patterns observed near the base and surface are directly linked to the SMB and BMB fields. Simply adjusting the SMB and BMB fields using the change in surface elevation after initialisation does not, however, suffice for inferring the correct boundary conditions. We have therefore first adjusted A and n in the Glen's flow law (J. Glen, 1958). The parameter n has an influence on the proportions of the dome shape of the ice rise as shown in, for example, Gillet-Chaulet et al. (2011). A range of Arrhenius factors, A, then need to be tested with the various Glen's flow law exponents, n, in order to obtain an optimal ice rise geometry. A further source of uncertainty is in the basal friction parameterisation. Assuming that there is negligible basal sliding where there is substantial horizontal divergence of ice flow, an adjustment of the basal friction parameter can be made until there is sufficient thinning of ice in the talweg and no thinning elsewhere. We acknowledge that although we aim to independently adjust the ice flow parameterisations and boundary conditions they are none-the-less dependent on one-another. We argue, however, that with the steps we have taken in model calibration and comparison with isochrones, we have moved a step closer to independently determining model parameters.

6 Conclusions

We have introduced a new three-dimensional ice-rise modelling framework that includes an ice rise, a grounding line, and the surrounding ice shelf. This framework allows us to compare the modelled three-dimensional stratigraphy with the observed stratigraphy. The modelling framework presented here can be transferred as is to other ice rises of interest to predict the age-depth fields prior to ice-core drilling and also to continue constraining ice-flow parameters relevant for continent-wide simulations. Overall, we find that the modelled stratigraphy of Derwael Ice Rise matches well with observed stratigraphy except in regions where there is uncertainty in the bed elevation. We predict 8000 year old ice at 95 % depth and spatial age gradients at intermediate depth are significant reflecting the spatial variability in SMB. Observed arches in the ice-rise flanks cannot be reproduced and are likely a remnant of a former ice-divide triple junction that has disappeared in the last 100 years.

The presented modelling framework provides a blueprint for the simulation of other ice rises with Glen's flow exponents of $n = 3$ and $n = 4$ to make comparisons with ice cores or observational stratigraphy with the hopes of narrowing down uncertainties in other model parameters in the future, such as temperature and grain size. Simulations with differing $n = 3$ and $n = 4$ broadly result in similar velocity and age-depth fields if the temperature dependent viscosity factors are tuned accordingly. Exceptions are areas close to the ice divide, the peripherial shear zones and in the ice close to the ice-bed interface, helping to establish limits on the strain rates that permit viscous flow. Furthermore, this framework is a valuable first step towards testing and constraining various physical processes such as fracturing and anisotropy, perhaps constrained with quad-polarimetric radar measurements (Ershadi et al., 2022).

Open Research Section

The code for the simulations can be found at `https://github.com/henryclara/Derwael/` and the code to produce the figures in the paper can be found at `https://github.com/henryclara/DerwaelAccompanyingCode`. The data for producing the figures and the data used as input to the model can be found at `https://nc-geophysik.guz.uni-tuebingen.de/index.php/s/7PdWiGeFJdFGMKH`.

Acknowledgments

C. Henry was supported by the Deutsche Forschungsgemeinschaft (DFG) in the framework of the priority programme 1158 "Antarctic Research with comparative investigations in Arctic ice areas" by a grant SCHA 2139/1-1. C. Schannwell was supported by the German Federal Ministry of Education and Research (BMBF) as a Research for Sustainability initiative (FONA) through the PalMod project under the grant number 01LP1915C. R. Drews and V. Višnjević were supported by an Emmy Noether Grant of the Deutsche Forschungsgemeinschaft (DR 822/3-1). This work used resources of the Deutsches Klimarechenzentrum (DKRZ) granted by its Scientific Steering Committee (WLA) under project ID bm1164.

References

Bons, P. D., Jansen, D., Mundel, F., Bauer, C. C., Binder, T., Eisen, O., ... others (2016). Converging flow and anisotropy cause large-scale folding in greenland's ice sheet. *Nature communications*, *7*(1), 1–6.

Bons, P. D., Kleiner, T., Llorens, M.-G., Prior, D. J., Sachau, T., Weikusat, I., & Jansen, D. (2018). Greenland ice sheet: Higher nonlinearity of ice flow significantly reduces estimated basal motion. *Geophysical Research Letters*, *45*(13), 6542–6548.

Born, A., & Robinson, A. (2021). Modeling the greenland englacial stratigraphy. *The Cryosphere*, *15*(9), 4539–4556.

Budd, W., & Jacka, T. (1989). A review of ice rheology for ice sheet modelling. *Cold Regions Science and Technology*, *16*(2), 107-144. Retrieved from `https://www.sciencedirect.com/science/article/pii/0165232X89900141` doi: https://doi.org/10.1016/0165-232X(89)90014-1

Callens, D., Drews, R., Witrant, E., Philippe, M., & Pattyn, F. (2016, June). Temporally stable surface mass balance asymmetry across an ice rise derived from radar internal reflection horizons through inverse modeling. *Journal of Glaciology*, *62*(233), 525–534. Retrieved 2022-01-13, from `https://www.cambridge.org/core/product/identifier/S0022143016000411/type/journal_article` doi: 10.1017/jog.2016.41

Callens, D., Matsuoka, K., Steinhage, D., Smith, B., Witrant, E., & Pattyn, F. (2014, May). Transition of flow regime along a marine-terminating outlet glacier in East Antarctica. *The Cryosphere*, *8*(3), 867–875. Retrieved 2021-11-21, from `https://tc.copernicus.org/articles/8/867/2014/` doi: 10.5194/tc-8-867-2014

Cavitte, M. G., Goosse, H., Wauthy, S., Kausch, T., Tison, J.-L., Van Liefferinge, B., ... Claeys, P. (2022). From ice core to ground-penetrating radar: representativeness of smb at three ice rises along the princess ragnhild coast, east antarctica. *Journal of Glaciology*, *68*(272), 1221–1233. doi: 10.1017/jog.2022.39

Comiso, J. C. (2000, May). Variability and trends in antarctic surface temperatures from in situ and satellite infrared measurements. *Journal of Climate*, *13*(10), 1674–1696. Retrieved from `http://journals.ametsoc.org/doi/10.1175/1520-0442(2000)013<1674:VATIAS>2.0.CO;2` doi: 10.1175/1520-0442(2000)013⟨1674:VATIAS⟩2.0.CO;2

Drews, R., Matsuoka, K., Martín, C., Callens, D., Bergeot, N., & Pattyn, F. (2015, March). Evolution of Derwael Ice Rise in Dronning Maud Land, Antarctica, over the last millennia. *Journal of Geophysical Research: Earth Surface*, *120*(3), 564–579. Retrieved 2021-08-16, from `http://doi.wiley.com/10.1002/2014JF003246` doi: 10.1002/2014JF003246

Drews, R., Schannwell, C., Ehlers, T., Gladstone, R., Pattyn, F., & Matsuoka, K. (2020). Atmospheric and oceanographic signatures in the ice shelf channel morphology of roi baudouin ice shelf, east antarctica, inferred from radar data. *Journal of Geophysical Research: Earth Surface*, *125*(7), e2020JF005587.

Ershadi, M. R., Drews, R., Martín, C., Eisen, O., Ritz, C., Corr, H., … Mulvaney, R. (2022). Polarimetric radar reveals the spatial distribution of ice fabric at domes and divides in east antarctica. *The Cryosphere*, *16*(5), 1719–1739. Retrieved from `https://tc.copernicus.org/articles/16/1719/2022/` doi: 10.5194/tc-16-1719-2022

Favier, L., & Pattyn, F. (2015, June). Antarctic ice rise formation, evolution, and stability. *Geophysical Research Letters*, *42*(11), 4456–4463. Retrieved 2021-08-16, from `https://onlinelibrary.wiley.com/doi/abs/10.1002/2015GL064195` doi: 10.1002/2015GL064195

Favier, L., Pattyn, F., Berger, S., & Drews, R. (2016, November). Dynamic influence of pinning points on marine ice-sheet stability: a numerical study in Dronning Maud Land, East Antarctica. *The Cryosphere*, *10*(6), 2623–2635. Retrieved 2021-12-09, from `https://tc.copernicus.org/articles/10/2623/2016/` doi: 10.5194/tc-10-2623-2016

Franke, S., Bons, P. D., Westhoff, J., Weikusat, I., Binder, T., Streng, K., … others (2022). Holocene ice-stream shutdown and drainage basin reconfiguration in northeast greenland. *Nature Geoscience*, 1–7.

Gagliardini, O., Zwinger, T., Gillet-Chaulet, F., Durand, G., Favier, L., de Fleurian, B., … Thies, J. (2013, August). Capabilities and performance of Elmer/Ice, a new-generation ice sheet model. *Geoscientific Model Development*, *6*(4), 1299–1318. Retrieved 2021-08-16, from `https://gmd.copernicus.org/articles/6/1299/2013/` doi: 10.5194/gmd-6-1299-2013

Gillet-Chaulet, F., & Hindmarsh, R. C. (2011). Flow at ice-divide triple junctions: 1. three-dimensional full-stokes modeling. *Journal of Geophysical Research: Earth Surface*, *116*(F2).

Gillet-Chaulet, F., Hindmarsh, R. C. A., Corr, H. F. J., King, E. C., & Jenkins, A. (2011, December). *In-situ* quantification of ice rheology and direct measurement of the Raymond Effect at Summit, Greenland using a phase-sensitive radar. *Geophysical Research Letters*, *38*(24), n/a–n/a. Retrieved 2021-11-21, from `http://doi.wiley.com/10.1029/2011GL049843` doi: 10.1029/2011GL049843

Glen, J. (1958). The flow law of ice: A discussion of the assumptions made in glacier theory, their experimental foundations and consequences. *IASH Publ*, *47*(171), e183.

Glen, J. W. (1955). The creep of polycrystalline ice. *Proceedings of the Royal Society of London. Series A. Mathematical and Physical Sciences*, *228*(1175), 519–538.

Goel, V., Martín, C., & Matsuoka, K. (2018). Ice-rise stratigraphy reveals changes in surface mass balance over the last millennia in dronning maud land. *Journal of*

Glaciology, *64*(248), 932–942. doi: 10.1017/jog.2018.81

Goldsby, D. L. (2006). Superplastic flow of ice relevant to glacier and ice-sheet mechanics. *Glacier science and environmental change*, 308–314.

Goldsby, D. L., & Kohlstedt, D. L. (2001). Superplastic deformation of ice: Experimental observations. *Journal of Geophysical Research: Solid Earth*, *106*(B6), 11017–11030.

Henry, A. C. J., Drews, R., Schannwell, C., & Višnjević, V. (2022). Hysteretic evolution of ice rises and ice rumples in response to variations in sea level. *The Cryosphere*, *16*(9), 3889–3905. Retrieved from `https://tc.copernicus.org/articles/16/3889/2022/` doi: 10.5194/tc-16-3889-2022

Hindmarsh, R. C., King, E. C., Mulvaney, R., Corr, H. F., Hiess, G., & Gillet-Chaulet, F. (2011). Flow at ice-divide triple junctions: 2. three-dimensional views of isochrone architecture from ice-penetrating radar surveys. *Journal of Geophysical Research: Earth Surface*, *116*(F2).

Jezek, K. C. (2003). Observing the antarctic ice sheet using the radarsat-1 synthetic aperture radar. *Polar Geography*, *27*(3), 197-209. Retrieved from `https://doi.org/10.1080/789610167` doi: 10.1080/789610167

Koch, I., Drews, R., Franke, S., Jansen, D., Oraschewski, F. M., Muhle, L., ... Eisen, O. (n.d.). Radar internal reflection horizons from multisystem data reflect ice dynamic and surface accumulation history along the princess ragnhild coast, dronning maud land, east antarctica [in review]. *Journal of Glaciology*.

Koch, I., Drews, R., Muhle, L. S., Franke, S., Jansen, D., Oraschewski, F., ... Eisen, O. (n.d.). Internal reflection horizons of ice shelves and ice rises in eastern dronning maud land (east antarctica) from multisystem radio-echo sounding data [in review]. *PANGAEA*. doi: https://doi.pangaea.de/10.1594/PANGAEA.950383

Martín, C., & Gudmundsson, G. H. (2012). Effects of nonlinear rheology, temperature and anisotropy on the relationship between age and depth at ice divides. *The Cryosphere*, *6*(5), 1221–1229. Retrieved from `https://tc.copernicus.org/articles/6/1221/2012/` doi: 10.5194/tc-6-1221-2012

Martín, C., Gudmundsson, G. H., & King, E. C. (2014). Modelling of Kealey Ice Rise, Antarctica, reveals stable ice-flow conditions in East Ellsworth Land over millennia. *Journal of Glaciology*, *60*(219), 139–146. Retrieved 2021-08-16, from `https://www.cambridge.org/core/product/identifier/S0022143000203286/type/journal_article` doi: 10.3189/2014JoG13J089

Martín, C., Hindmarsh, R. C. A., & Navarro, F. J. (2006). Dating ice flow change near the flow divide at Roosevelt Island, Antarctica, by using a thermomechanical model to predict radar stratigraphy. *Journal of Geophysical Research*, *111*(F1), F01011. Retrieved 2021-08-16, from `http://doi.wiley.com/10.1029/2005JF000326` doi: 10.1029/2005JF000326

Martín, C., Hindmarsh, R. C. A., & Navarro, F. J. (2009, April). On the effects of divide migration, along-ridge flow, and basal sliding on isochrones near an ice divide. *Journal of Geophysical Research*, *114*(F2), F02006. Retrieved 2021-08-16, from `http://doi.wiley.com/10.1029/2008JF001025` doi: 10.1029/2008JF001025

Millstein, J. D., Minchew, B. M., & Pegler, S. S. (2022). Ice viscosity is more sensitive to stress than commonly assumed. *Communications Earth & Environment*, *3*(1), 1–7.

Morlighem, M., Rignot, E., Binder, T., Blankenship, D., Drews, R., Eagles, G., ... others (2020). Deep glacial troughs and stabilizing ridges unveiled beneath the margins of the antarctic ice sheet. *Nature Geoscience*, *13*(2), 132–137.

Nereson, N. A., Raymond, C. F., Waddington, E. D., & Jacobel, R. W. (1998). Migration of the siple dome ice divide, west antarctica. *Journal of Glaciology*, *44*(148), 643–652. Retrieved from `https://www.cambridge.org/core/product/identifier/S0022143000002148/type/journal_article` doi:

10.3189/S0022143000002148
Philippe, M., Tison, J.-L., Fjøsne, K., Hubbard, B., Kjær, H. A., Lenaerts, J., ... others (2016). Ice core evidence for a 20th century increase in surface mass balance in coastal dronning maud land, east antarctica. *The Cryosphere*, *10*(5), 2501–2516.
Raymond, C. F. (1983). Deformation in the Vicinity of Ice Divides. *Journal of Glaciology*, *29*(103), 357–373. Retrieved 2021-08-16, from https://www.cambridge.org/core/product/identifier/S0022143000030288/type/journal_article doi: 10.1017/S0022143000030288
Rignot, J. M., E., & Scheuchl., B. (2017). *Measures insar-based antarctica ice velocity map, version 2.* NASA National Snow and Ice Data Center Distributed Active Archive Center. Retrieved from https://nsidc.org/data/NSIDC-0484/versions/2 doi: 10.5067/D7GK8F5J8M8R
Ritz, C. (1987). *Time dependent boundary conditions for calculation of temperature fields in ice sheets. in: E. d. waddington and j. s. walder (eds.), the physical basis of ice sheet modelling, iahs publication no. 170, pp. 207–216.* IAHS Press, Wallingford, UK.
Schannwell, C., Drews, R., Ehlers, T. A., Eisen, O., Mayer, C., & Gillet-Chaulet, F. (2019, October). Kinematic response of ice-rise divides to changes in ocean and atmosphere forcing. *The Cryosphere*, *13*(10), 2673–2691. Retrieved 2021-11-21, from https://tc.copernicus.org/articles/13/2673/2019/ doi: 10.5194/tc-13-2673-2019
Schannwell, C., Drews, R., Ehlers, T. A., Eisen, O., Mayer, C., Malinen, M., ... Eisermann, H. (2020, November). Quantifying the effect of ocean bed properties on ice sheet geometry over 40 000 years with a full-Stokes model. *The Cryosphere*, *14*(11), 3917–3934. Retrieved 2021-11-21, from https://tc.copernicus.org/articles/14/3917/2020/ doi: 10.5194/tc-14-3917-2020
Sutter, J., Fischer, H., & Eisen, O. (2021). Investigating the internal structure of the antarctic ice sheet: the utility of isochrones for spatiotemporal ice-sheet model calibration. *The Cryosphere*, *15*(8), 3839–3860.
van den Broeke, M. R. (2019). *RACMO2.3p1 annual surface mass balance Antarctica (1979-2014)* [data set]. PANGAEA. Retrieved from https://doi.org/10.1594/PANGAEA.896940 doi: 10.1594/PANGAEA.896940
Waddington, E. D., Neumann, T. A., Koutnik, M. R., Marshall, H.-P., & Morse, D. L. (2007). Inference of accumulation-rate patterns from deep layers in glaciers and ice sheets. *Journal of Glaciology*, *53*(183), 694–712. doi: 10.3189/002214307784409351
Weertman, J. (1957). On the sliding of glaciers. *Journal of Glaciology*, *3*(21), 33–38. doi: 10.3189/S0022143000024709
Weertman, J. (1983, May). Creep deformation of ice. *Annual Review of Earth and Planetary Sciences*, *11*(1), 215–240. Retrieved from https://www.annualreviews.org/doi/10.1146/annurev.ea.11.050183.001243 doi: 10.1146/annurev.ea.11.050183.001243
Zeitz, M., Levermann, A., & Winkelmann, R. (2020). Sensitivity of ice loss to uncertainty in flow law parameters in an idealized one-dimensional geometry. *The Cryosphere*, *14*(10), 3537–3550.
Zwinger, T., Greve, R., Gagliardini, O., Shiraiwa, T., & Lyly, M. (2007). A full stokes-flow thermo-mechanical model for firn and ice applied to the gorshkov crater glacier, kamchatka. *Annals of Glaciology*, *45*, 29–37.
Zwinger, T., & Moore, J. C. (2009). Diagnostic and prognostic simulations with a full stokes model accounting for superimposed ice of midtre lovénbreen, svalbard. *The Cryosphere*, *3*(2), 217–229. Retrieved from https://tc.copernicus.org/articles/3/217/2009/ doi: 10.5194/tc-3-217-2009

Predicting the three-dimensional age-depth field of an ice rise

A. C. J. Henry[1,2,3], C. Schannwell[1], V. Višnjević[2], J. Millstein[4], P. D. Bons[2], O. Eisen[5,6], R. Drews[2]

[1]Max Planck Institute for Meteorology, Hamburg, Germany
[2]Department of Geosciences, University of Tübingen, Tübingen, Germany
[3]International Max Planck Research School on Earth System Modelling, Max Planck Institute for Meteorology, Hamburg, Germany
[4]Massachusetts Institute of Technology—Woods Hole Oceanographic Institute Joint Program in Oceanography/Applied Ocean Science and Engineering, Cambridge, MA, USA
[5]Alfred Wegener Institute Helmholtz Centre for Polar and Marine Research, Bremerhaven, Germany
[6]University of Bremen, Bremen, Germany

Key Points:

- First three-dimensional simulations of the stratigraphy of an ice rise allowing comparison of model results with radar observations.
- Choice of the Glen's flow law exponent influences deformation in the grounding zones.
- Reduction in surface elevation at the divide relative to observations points at missing processes in the model such as anisotropy.

Corresponding author: A. C. J. Henry, `clara.henry@mpimet.mpg.de`

Abstract

Ice rises situated around the perimeter of Antarctica buttress ice flow and contain information about the past climate and changes in flow regime. Moreover, ice rises contain convergent and divergent flow regimes, and both floating and grounded ice over comparatively small spatial scales, meaning they are ideal locations to study ice-flow dynamics. Here, we introduce a new modelling framework that permits the comparison between modelled and observed stratigraphy. A thermo-mechanically coupled, isotropic, Stokes ice flow model with a dynamic grounding line is used (Elmer/Ice). The result is the simulated age-depth field of a three-dimensional, steady-state ice rise which is dynamically coupled to the surrounding ice shelf. Applying the model to Derwael Ice Rise, results show a good match between observed and modelled stratigraphy over most of the ice rise and predict approximately 8000 year old ice at a depth of 95 %. Differences in the prediction of age between simulations using Glen's flow law exponents of $n = 3$ and $n = 4$ are generally small (< 5 % over most areas). In the ice rise shear zones, large differences in shear strain rates in the velocity direction are found between the $n = 3$ and the $n = 4$ simulations. Our simulations indicate that a Glen's flow law exponent of $n = 4$ may be better suited when modelling ice rises due to a steady-state geometry which is closer to the observed geometry. Our three-dimensional modelling framework can easily be transferred to other ice rises and has relevance for researchers interested in ice core dating and understanding ice-flow re-organisation.

Plain Language Summary

Ice rises are features which form in coastal Antarctica when the ice shelf comes into contact with the bathymmetry. These features provide a backstress on the ice shelf and can influence grounding line position. We simulate an ice rise in East Antarctica called Derwael Ice Rise, outlining the steps necessary to model the three-dimensional stratigraphy of an ice rise and compare the modelled stratigraphy with observed stratigraphy derived from radar measurements. Comparisons between the observed and modelled stratigraphy allow us to validate boundary conditions and the parameterisations used in our model. This work is relevant as a blueprint for simulating other ice rises for those interested in comparison with ice core records, and investigating ice rises formation and evolution.

1 Introduction

Ice rises form where ice shelves ground locally on topographic highs in the bathymmetry and are important in coastal Antarctic ice flow dynamics as they regulate the flow of ice towards the ocean (Favier & Pattyn, 2015; Favier et al., 2016; Henry et al., 2022). Moreover, ice rises are valuable as a climate archive because they often provide high-resolution and undisturbed records throughout the Holocene. Ice-core drill sites are often located at local summits to avoid lateral flow. However, it is a significant challenge to predict the age-depth fields prior to drilling. This is due to strong variations in surface mass balance (SMB, Cavitte et al. (2022)) and also because the ice-flow regimes change over a few tens of kilometres. Divide flow at the summit (where arches in the internal stratigraphy may form) turns into flank flow, and finally to the grounding zone where coupling with the surrounding ice shelves takes place. Compared to Antarctica's interior, ice rises at the coast are comparatively easy to reach and consequently a number of them , Derwael Ice Rise being one of them, have been densely surveyed with radar to image the isochronal stratigraphy. This enables the comparison of model predictions across various flow regimes with observations which can help calibrate model parameters such as Glen's flow law exponent, the fundamental constitutive relation for ice flow.

The non-Newtonian flow of ice (J. W. Glen, 1955; Weertman, 1983; Budd & Jacka, 1989) results in Raymond arches (Raymond, 1983) which form in the stratigraphy under the ice-rise divides and have been used to estimate how stationary ice-divide flow is. This effect can be dampened, for example, by along-ridge flow or changing conditions, thus inhibiting their formation. Under a changing climate, the geometry of an ice rise often changes, thereby causing a change in the isochronal structure (Nereson et al., 1998; Martín et al., 2009). The onset of stability of an ice rise is indicated by the amplitude of the Raymond arches and a change in the size of an ice rise is indicated by the migration of Raymond arches visible in the stratigraphy as side arches or tilted anticline stacks. Simulations of the stratigraphy of specific ice rises have thus far been performed in two dimensions (Martín et al., 2006, 2009, 2014; Drews et al., 2015; Goel et al., 2018), with Gillet-Chaulet and Hindmarsh (2011) performing simulations of the stratigraphy of an idealised ice rise in three dimensions without the inclusion of the surrounding ice shelf.

In this paper, we build on previous ice-rise modelling studies (Martín et al., 2009; Drews et al., 2015; Schannwell et al., 2019, 2020) and extend them by introducing a modelling framework that allows us to model ice rises including the surrounding ice shelves and their stratigraphy in three dimensions. This not only permits the prediction of the stratigraphy, but also accounts for three-dimensional effects that are of importance for comparisons with radar observations and ice cores. Whilst having proven important in the development of an understanding of Raymond arches, the two-dimensional studies do not allow for along-ridge flow. Studies investigating the observed stratigraphy in shear zones (Franke et al., 2022) and zones of convergence (Bons et al., 2016) have been performed, but a comparison between observed and modelled stratigraphy in such settings has not yet been performed. In idealised simulations (Hindmarsh et al., 2011; Gillet-Chaulet et al., 2011), it has been shown that along-ridge flow has a dampening effect on Raymond arch evolution. Where these simulations lack, however, is in the use of idealised boundary forcing conditions, which do not sufficiently produce the differing flow regime conditions on the stoss and lee sides of an ice rise.

The introduction of our new modelling framework provides a blueprint for modelling a real-world ice rise in three dimensions using the thermo-mechanically coupled model Elmer/Ice (Gagliardini et al., 2013) in order to predict the age field ice-rise wide. We investigate how robust those results are compared to observations with two Glen's flow law exponents. We choose to compare simulations using the typical exponent of $n = 3$ with simulations using an exponent of $n = 4$, closer to the value of $n = 4.1 \pm 0.4$ found to work best for Antarctic ice shelves (Millstein et al., 2022) and similar values suggested by Bons et al. (2018) for Greenland. The conversion from using a Glen's flow law with an exponent of $n = 3$ to an exponent of $n = 4$ is made using an initial scalar stress estimate along with simulations for the evaluation of an appropriate Arrhenius prefactor for $n = 4$.

The three-dimensional, steady-state simulations presented here have relevance for comparisons with ice cores and in the context of understanding the link between isochronal structures and changes in ice geometry and external forcing. Steady-state simulations allow the deduction of changes due to misfits and provide an important step towards the use of ice rises as a constraint for paleo ice-sheet simulations. This study not only successfully demonstrates three-dimensional modelling to bridge Stokes models with observed radar stratigraphy, but also delves into the implications of model parameter choice by exploiting variables in Glen's flow law.

2 Derwael Ice Rise

Derwael Ice Rise has a grounded area of roughly 1050 km^2 and is an isle-type ice rise with a ridge divide. The grounded area has a maximum width of roughly 35 km perpendicular to the predominant flow direction of the ice shelf. The ice rise has a maxi-

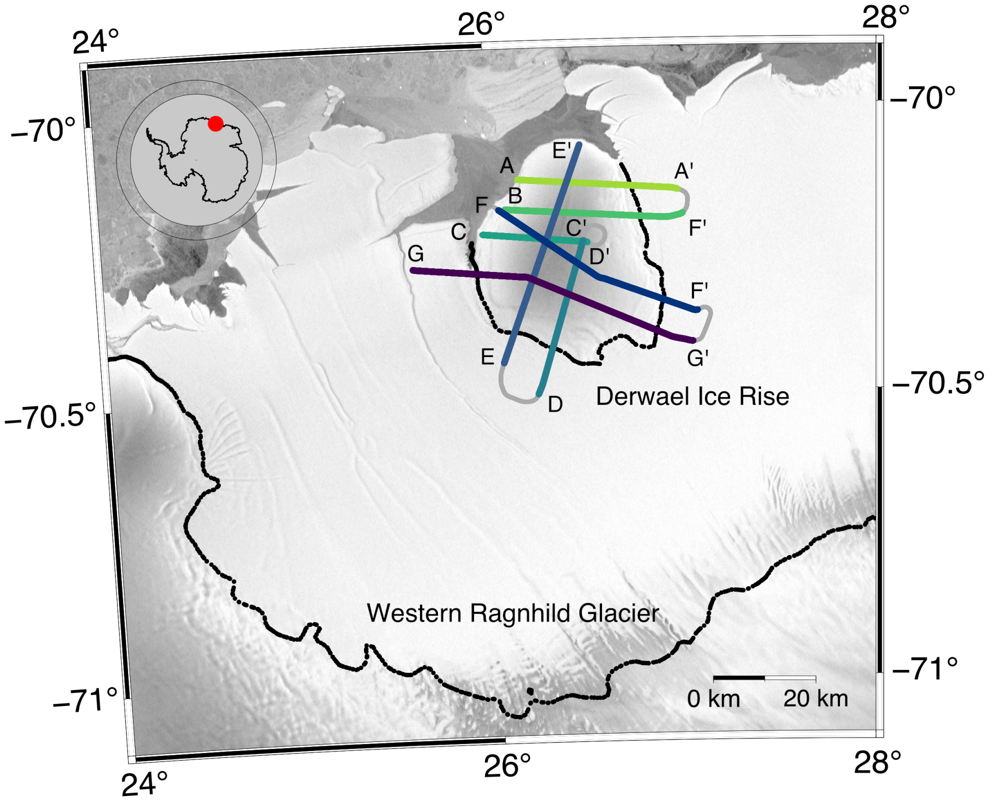

Figure 1. The location of Derwael Ice Rise within the Roi Baudouin Ice Shelf in East Antarctica. The coloured line segments $A - A'$ to $G - G'$ indicate the locations of radar measurements taken using airborne radar. The continental and ice rise grounding lines are indicated by the black lines. The RADARSAT mosaic (Jezek, 2003) is shown in the background, and the grounding line (black dots) is from Morlighem et al. (2020).

mum ice thickness of roughly 630 m with an estimated accuracy of 5 % (Morlighem et al., 2020) and is thickest in the south of the ice rise, where there is convergence of flow from the ice rise and the ice shelf. The maximum ice thickness at the ridge divide is roughly 540. We choose Derwael Ice Rise because of the availability of radar data across the ice rise divide and the shear margins, and also because Derwael Ice Rise is close to steady-state, perhaps with some current thinning (Drews et al., 2015; Callens et al., 2016). Derwael Ice Rise has well expressed isochrone arches beneath the ridge divide. A pecularity is, that arches (referred to as side arches later on) also occur in the south-eastern flanks close to the divide (Drews et al., 2015). An ice rumple is located in the north-western corner of the domain.

3 Methods

The model setup is based on Henry et al. (2022), and here we extend the framework to real-world geometries. In the following sections, we describe the required modifications to accomplish this. We use the finite element software Elmer/Ice (Gagliardini et al., 2013) to solve the Stokes equations. Here, we describe the coupled equations, model parameters boundary conditions and mesh resolution.

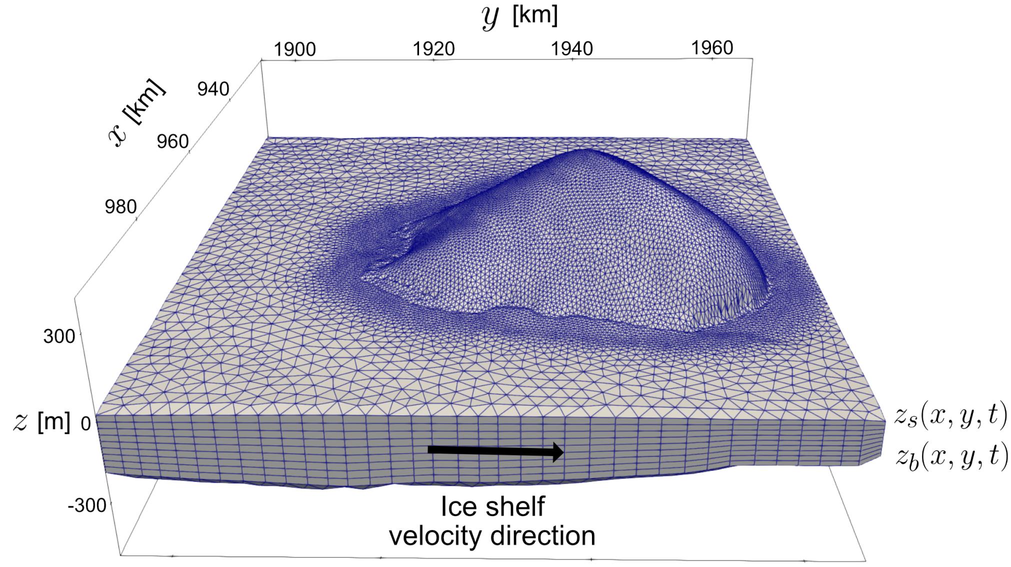

Figure 2. The model set up with horizontal distances in Antarctic polar stereographic projection. The area encompassing the ice rise has a characteristic resolution of 500 m and the surrounding area has a resolution of 2000 m. The upper ice surface is denoted by $z_s = z_s(x, y, t)$ and the lower ice surface by $z_b = z_b(x, y, t)$, where x and y are the horizontal directions and z is the vertical direction relative to sea level. Note: for visualisation, the vertical is scaled by a factor of 30.

Table 1. List of parameters used in the simulations

Parameter	Symbol	Value	Unit
Basal friction exponent	m	1/3	
Local ocean density	ρ_w	1000	kg m^{-3}
Ice density	ρ_i	900	kg m^{-3}
Gravity	g	9.8	m s^{-2}
Universal gas constant	R	8.314	mol^{-1}K^{-1}
Geothermal heat flux	ϕ_q	50	mWm^{-2}
Basal melt parameter	b_0	0.95	ma^{-1}

3.1 Governing equations

The Stokes equations,

$$\boldsymbol{\nabla} \cdot (\boldsymbol{\tau} - P\mathbf{I}) + \rho_i \mathbf{g} = 0, \tag{1}$$

describe the flow of ice, where $\boldsymbol{\tau}$ is the deviatoric stress tensor, P is the pressure, $\mathbf{I}$ is the identity matrix, ρ_i is the ice density and $\mathbf{g} = -g\hat{\mathbf{e}}_z$ is the gravitational acceleration. The ice is subject to an incompressibility condition,

$$\boldsymbol{\nabla} \cdot \mathbf{u} = 0. \tag{2}$$

The Glen's power flow law,

$$\boldsymbol{\tau} = 2\eta\dot{\boldsymbol{\varepsilon}}, \tag{3}$$

describes the nonlinear dependence between the strain rate tensor, $\dot{\boldsymbol{\varepsilon}}$, and the deviatoric stress tensor. The effective viscosity, η, is

$$\eta = \frac{1}{2} A(T)^{-1/n} \dot{\varepsilon}_e^{(1-n)/n}, \tag{4}$$

where $A(T)$ is the ice fluidity which is dependent on temperature, T, and is described in detail below. The effective strain rate, $\dot{\varepsilon}_e^2$, is the square of the second invariant of the strain rate tensor, $\dot{\boldsymbol{\varepsilon}}$. As in Gagliardini et al. (2013), the temperature of the ice evolves subject to

$$\rho_i c_v \left(\frac{\delta T}{\delta t} + \mathbf{u} \cdot \boldsymbol{\nabla} T \right) = \nabla \cdot (\kappa \boldsymbol{\nabla} T) + \mathbf{D} : \boldsymbol{\sigma}, \tag{5}$$

where : is the double inner product,

$$c_v = 146.3 + 7.253T \tag{6}$$

is the specific heat capacity of the ice and

$$\kappa = 9.828 \exp\big(-5.7 \times 10^{-03} T\big) \tag{7}$$

is the thermal conductivity (Ritz, 1987). The temperature is coupled to the Glen's flow law using an Arrhenius law

$$A(T, p) = E A_0 \exp(-Q/RT), \tag{8}$$

where A_0 is a constant pre-factor, Q is the activation energy and R is the universal gas constant. The Arrhenius law is multiplied by a constant, E, called an enhancement factor, in order to obtain an optimal coefficient in the Arrhenius law. The combination of the parameters A_0 and E are used in ice sheet modelling to account for effects such as grain size, crystal orientation, impurities, porosity and water content. An exploration of the influence of each process is beyond the scope of this study, but we will note here that processes which soften ice cause either an increase in the parameter A_0 or E. For calculating the equivalent Arrhenius factor for a Glen's flow law exponent of $n = 3$, we take a similar approach to Zeitz et al. (2020) and use a first estimate of the stress magnitude of $[\tau_0] = 0.25 \times 10^6$ Pa, so that

$$A_0\big|_{n=4} \exp\big(-Q\big|_{n=4}\big) = \frac{A_0\big|_{n=3} \exp\big(-Q\big|_{n=3}\big)}{[\tau_0]}. \tag{9}$$

The first estimate of τ_0 is to compensate for the multiplication of an additional deviatoric stress tensor in Glen's flow law. The upper surface temperature is set equal to the temperature field data (Comiso, 2000). Initially, a linear temperature profile from the lower ice surface to the upper ice surface is prescribed. During transient simulation, the upper and lower surface temperatures evolve subject to a Neumann boundary condition.

During initialisation, the lower ice surface temperature is prescribed to be the pressure melting point temperature,

$$T_p = 273.15 - \beta \rho_i g (z_s - z). \tag{10}$$

Here, β denotes the Clausius-Clapeyron constant, $\beta = 9.8 \times 10^{-8}$ K Pa^{-1} (Zwinger et al., 2007). In order to solve for the isochronal stratigraphy of the ice, the age of the ice is solved according to

$$\frac{\partial \psi}{\partial t} + \mathbf{u} \cdot \nabla(\psi) = 1 \tag{11}$$

where ψ is the age of the ice (Zwinger & Moore, 2009). Eq. 11 is solved using a semi-Lagrangian scheme implemented in Elmer/Ice (Martín & Gudmundsson, 2012).

The upper ice surface, $z = z_s(x, y, t)$, and the lower ice surface, $z = z_b(x, y, t)$, evolve subject to

$$\left(\frac{\partial}{\partial t} + \mathbf{u} \cdot \boldsymbol{\nabla} \right) (z - z_s) = \dot{a}_s, \tag{12}$$

and

$$\left(\frac{\partial}{\partial t} + \mathbf{u} \cdot \boldsymbol{\nabla} \right) (z - z_b) = \dot{a}_b, \tag{13}$$

respectively, where $\dot{a}_s = \dot{a}_s(x, y)$ is the ice-equivalent SMB. The basal melt rate, $\dot{a}_b = \dot{a}_b(x, y)$, is set to a suitable constant of 0.95 m a^{-1} which resulted in minimal adjustment of ice shelf thickness and grounding line position and is close to the average spatial value of 0.8 m a^{-1} across the Roi Baudouin Ice Shelf (Drews et al., 2020). The SMB, $\dot{a}_s$, is described in further detail below. Where ice is in contact with the bed, a non-linear Weertman friction law (Weertman, 1957) is used,

$$\boldsymbol{\tau}_b = -C |\mathbf{u}_b|^{m-1} \boldsymbol{u}_b, \tag{14}$$

where $\boldsymbol{\tau}_b$ is the basal shear stress, C is a constant friction coefficient, $\boldsymbol{u}_b$ is the velocity tangential to the bed, and m is the friction law exponent and has the value $m = 1/3$ in all simulations.

For all our simulations, we use a horizontal resolution of 500 m in the area encompassing the ice rise up to a distance from the grounding line of 5000 m and the surrounding area has a resolution of 2000 m (Fig. 2). In the vertical, the mesh is made up of 10 layers. The higher resolution is needed in order to better resolve the stratigraphy of the ice rise. The Elmer/Ice grounding line implementation *Discontinous* is used.

3.2 Observational data, initial conditions and boundary conditions

3.2.1 Observational stratigraphy

Airborne radar data were acquired in the 2018/19 Antarctic field season as part of the CHIPSM survey using the Polar 6 aircraft of the Alfred Wegener Institute with an ultrawideband radar (MCoRDS v5) and eight-element fuselage antenna array operating in the 150–520 MHz frequency range. Details on data processing and tracing of isochronal internal layers is laid out in (Koch, Drews, Franke, et al., n.d.), which use the same data set. Dating of the two shallowest internal layers along the radar profiles is based on an ice-core depth scale (Philippe et al., 2016) under the assumption of a steady-state age-depth relation (Koch, Drews, Franke, et al., n.d.). This yields a total of seven profiles across the ice rise (Fig. 1).

In order to make comparisons between the modelled isochronal stratigraphy and the observed internal reflection horizons possible, a density adjustment needs to be made. This can be done either by adjusting the modelled isochrone elevation to match the density profile of the real-world ice rise or vice versa. We choose the latter. The adjustment

Table 2. List of simulations

Simulation	n	E	Pre-factor 1 [Pa^{-n} a^{-1}]	Pre-factor 2 [Pa^{-n} a^{-1}]
n3E0.2	3	0.2	1.258×10^7	6.046×10^{22}
n3E0.4	3	0.4	1.258×10^7	6.046×10^{22}
n3E0.5	3	0.5	1.258×10^7	6.046×10^{22}
n3E0.6	3	0.6	1.258×10^7	6.046×10^{22}
n3E0.8	3	0.8	1.258×10^7	6.046×10^{22}
n3E1.0	3	1.0	1.258×10^7	6.046×10^{22}
n4E1.2	4	1.2	5.032×10^7	2.419×10^{23}
n4E1.6	4	1.6	5.032×10^7	2.419×10^{23}
n4E1.8	4	1.8	5.032×10^7	2.419×10^{23}
n4E2.0	4	2.0	5.032×10^7	2.419×10^{23}
n4E2.4	4	2.4	5.032×10^7	2.419×10^{23}
n4E2.8	4	2.8	5.032×10^7	2.419×10^{23}

results in isochrone elevations equivalent to a constant density of 900 kg m^{-3} and is calculated according to the density profile of Derwael Ice Rise in Callens et al. (2014). Throughout the paper, when referring to depth below surface in relation to observations, these are relative to the BedMachine surface elevation, adjusted to an equivalent of 900 kg m^{-3} as opposed to the 917 kg m^{-3} assumed in BedMachine. On the other hand, when referring to depth below surface in relation to model results, depths are relative to the steady-state modelled surface using a denisty of 900 kg m^{-3}. Note that this choice does not have an effect on the final comparison between the modelled and observed isochrones.

3.2.2 Surface and basal mass balances, velocity, bed and ice geometry

Over the ice rise, we derive the SMB along transects from the shallow radar stratigraphy using the standard approach of the shallow layer approximation (Waddington et al., 2007). Isochrones are dated using an ice core drilled at the summit (Philippe et al., 2016). Details of this are presented in (Koch, Drews, Franke, et al., n.d.) accompanied by the dataset (Koch, Drews, Muhle, et al., n.d.). We interpolated between radar transects using an interpolation scheme and merge the SMB field at the ice-rise edges with reanalysis data from RACMO2.3p1 mean annual SMB from the years 1979-2014 (van den Broeke, 2019). Including the SMB estimates from radar observations is a critical step in the analysis because the reanalysis data are too coarsely resolved on the ice rise. In order to avoid model drift due to uncorrected offsets in the SMB field, we correct the SMB field by subtracting it by the rate of change of the surface elevation after 50 years of simulation time.

At the domain boundary on the oceanward side of the ice rise, the ice is allowed to flow subject to hydrostatic pressure. At all other boundaries, depth-independent fluxes are prescribed and are derived from observed velocities (Rignot & Scheuchl., 2017). The bed elevation and the initial ice geometry is prescribed using BedMachine Antarctica data (Morlighem et al., 2020). When comparing BedMachine bed elevation with observations from our radar survey, we found significant mismatches of roughly 150 m in the north-eastern corner of Derwael Ice Rise (Fig. 4). This is surprising given that the radar survey is part of the BedMachine dataset. We see some interpolation artefacts where the grounded ice bed elevation dataset is merged with the bed elevation data below floating ice.

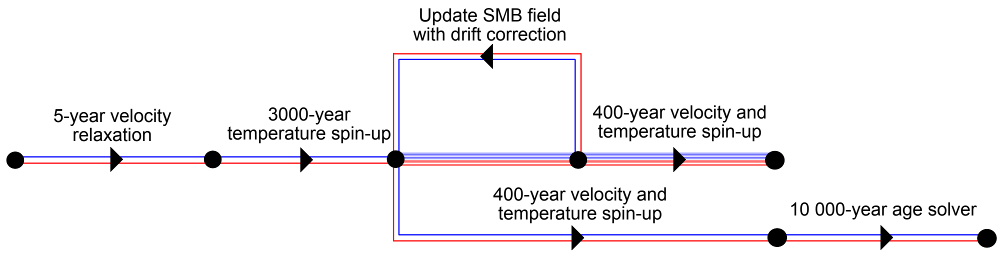

Figure 3. The schematic shows the spin-up procedure for the simulations in Table 2. The blue lines refer to the $n = 3$ simulations and the red lines refer to the $n = 4$ simulations. The black dots indicate the points when the simulation was restarted with a change in model set up as indicated by the schematic labels. Further details regarding the sequence of steps are given in Section 3.3.

3.3 Model spin-up procedure

In order to model the three-dimensional isochronal stratigraphy of an ice rise, the following steps are taken to spin-up the model. The details are as follows and can be seen in Fig. 3.

Step 1: Simulate the ice rise for 5 years with the Stokes, temperature, and upper and lower free surface solvers on for Glen's flow law exponents of $n = 3$ and $n = 4$.
Step 2: Spin up the temperature for 3000 years with the Stokes and free surface solvers off.
Step 3: Simulate with the chosen set of parameters (Table 2) for 400 years.
Step 4: Choose the optimal $n = 3$ and $n = 4$ simulation based on the least volume change (Fig. 6).
Step 5: Compute SMB from model drift after allowing the surface elevation to evolve for 50 years. The SMB is adjusted using the model drift over the grounded area and is incorporated with the combined stratigraphy-derived and RACMO2.3p1 SMB field. A Gaussian filter is applied to remove steep gradients.
Step 6: Simulate with the temperature, free surface and Stokes solvers activated for 400 years.
Step 7: Run the age solver with the Stokes, free surface and temperature solvers off for 10000 years.

4 Results

4.1 Model parameter choice and applied surface mass balance

In contrast to the SMB field from the RACMO2.3p1 simulation, the highest values of the stratigraphy-derived and drift-corrected SMB are concentrated in the centre of the ice rise (Fig. 5 in the Supporting Information). Here, the differences in spatial variation before and after the drift correction are evident, with the drift-corrected SMB being concentrated more towards the west of the ice rise. RACMO2.3p1 data shows higher values on the eastern and northern sides of the ice rise, whereas the stratigraphy-derived and drift-corrected SMB has higher values in the centre and on the south-western side of the ice rise. The results are close to mean SMB values of 0.47 ± 0.02 m w.e. a^{-1} (for comparison with our results, this is equivalent to 0.52 ± 0.02 m a^{-1} assuming an ice density of 900 kg m^{-3}) for the period 1816−2011 found by (Philippe et al., 2016), derived from an ice core at the summit of Derwael Ice Rise.

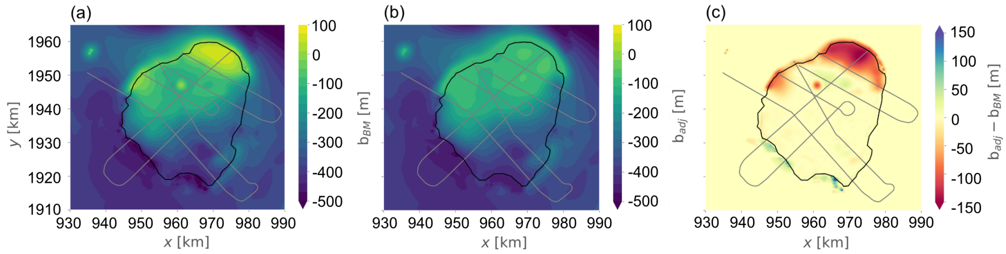

Figure 4. The BedMachine Antarctica bed elevation is shown in (a) and the adjusted bed elevation after re-interpolation and smoothing of unphysical anomalies is shown in (b). The difference between the adjusted bed elevation and the original BedMachine bed elevation is shown in (c). The grey lines show the location of radargrams with which the simulations are compared. The bed elevation data from these radar lines has been used in the BedMachine data.

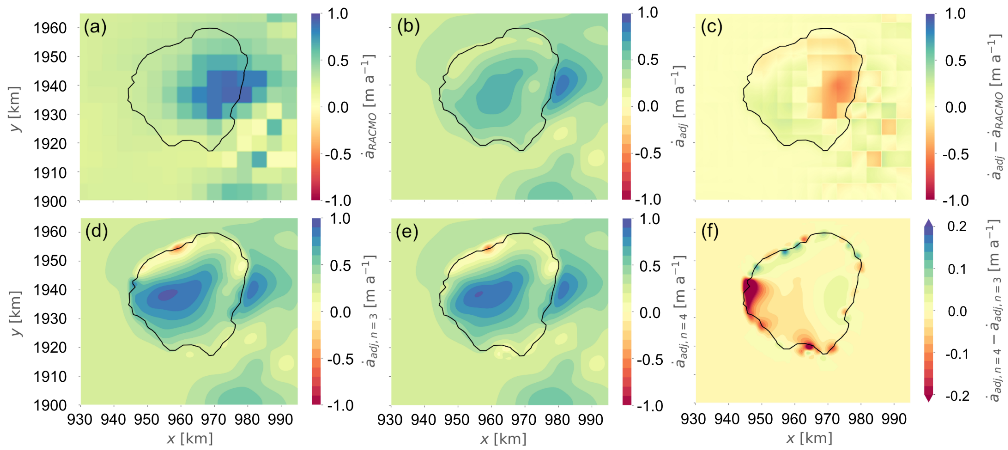

Figure 5. Surface mass balance (SMB) (a) based on RACMO2.3p1 data; (b) the adjusted product from a combination of stratigraphy-derived data in the grounded area and RACMO2.3p1 data in the surrounding area; (c) difference between the adjusted and the RACMO2.3p1 SMB. The SMB in (d) and (e) use a drift correction made with the $\partial z_s/\partial t$ field after a simulation time of 50 years for the $n = 3$ and the $n = 4$ simulations, respectively and (f) shows the difference in SMB between the $n = 3$ and $n = 4$ simulations for the stratigraphy-derived and drift-corrected SMB.

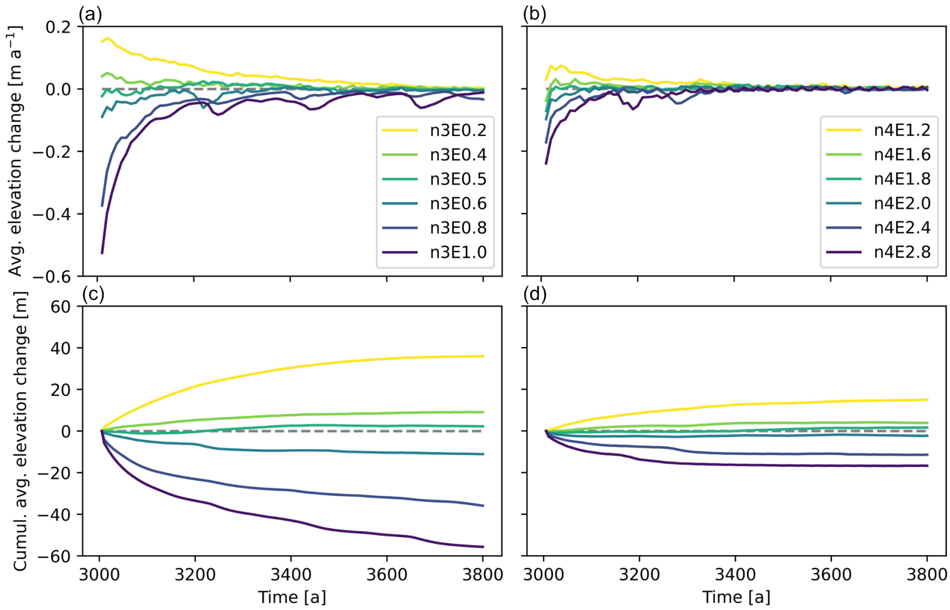

Figure 6. Elevation changes for different simulations: (a) and (b) show the average elevation changes, and (c) and (d) show the cumulative elevation changes for Glen's flow law exponents of $n = 3$ and $n = 4$, respectively, for varying enhancement factors. Legends indicate the different model runs in colour.

In order to find the optimal combination of parameters in the simulations of Derwael Ice Rise, an ensemble of simulations for various enhancement factors were performed. Here we note that in this work we take the enhancement factor to simply be a constant multiplier that adjusts the Arrhenius factor, A_0 and is equivalent to adjusting the Arrhenius pre-factor itself. As a performance evaluation metric in order to find the optimal enhancement factor, we use the change in surface elevation with respect to time across the grounded ice (Fig. 6), assuming that Derwael Ice Rise is in steady state. We found that an enhancement factor of $E = 0.5$ (simulation $n3E0.5$) produced an ice rise with the least cumulative volume change in the $n = 3$ simulations. For the $n = 4$ simulations, a corresponding enhancement factor of $E = 1.8$ (simulation $n4E1.8$) is found. Henceforth, we refer to the $n3E0.5$ and the $n4E1.8$ simulations simply as the $n = 3$ and $n = 4$ simulations, respectively. Large fluctuations seen in Fig. 6 (c) and (d) are due to sudden changes in grounding line position and temporary localised decreases in elevation. Simulations with an underestimated or overestimated enhancement factor result in elevation and volumetric changes.

In both the $n = 3$ and the $n = 4$ simulation, there is a slight reduction in ice thickness at the divide compared with the BedMachine data of roughly 15 m (corresponding to 3 % of the ice thickness at the divide). This reduction in ice thickness is less in the $n = 4$ than the $n = 3$ simulation. On the western side of the ice rise excess thinning of the ice occurs, whereas in all other grounding zones, too much thickening occurs. Comparing the elevation change between the $n = 3$ and $n = 4$ simulations (Fig. 8), it can be seen that the steady-state $n = 3$ simulation has a lower elevation in the centre of the ice rise than the $n = 4$ simulation. In the north-eastern flank of the ice rise, the $n = 3$ simulation has a lower steady-state surface elevation than the $n = 4$ simulation, but all other flanks show a tendency for a higher surface elevation in the case of the $n = 3$ simulation.

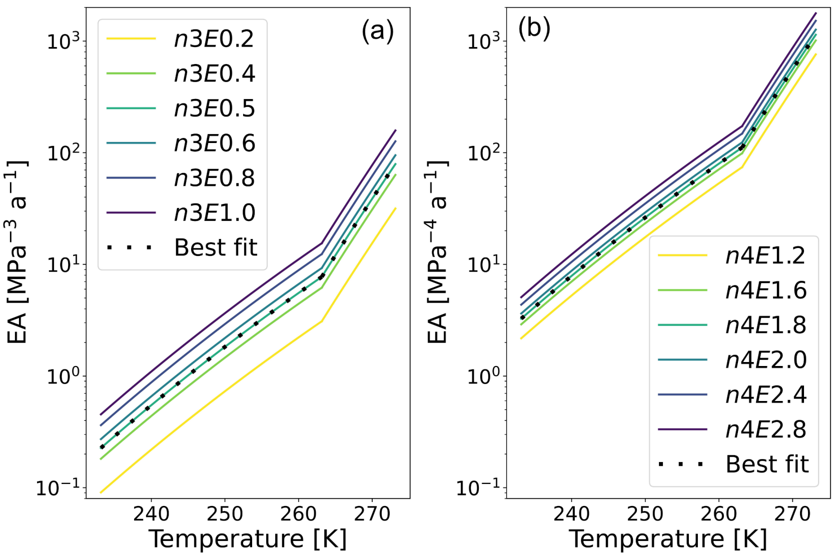

Figure 7. The relationship between the temperature and the Arrhenius law multiplied by varying enhancement factors, E; (a) corresponds with the $n = 3$ simulations and (b) with the $n = 4$ simulations. Note the y-axes have a logarithmic scale. In (a) and (b), the dotted lines indicate the most suitable combination of parameters for the simulations of Derwael Ice Rise.

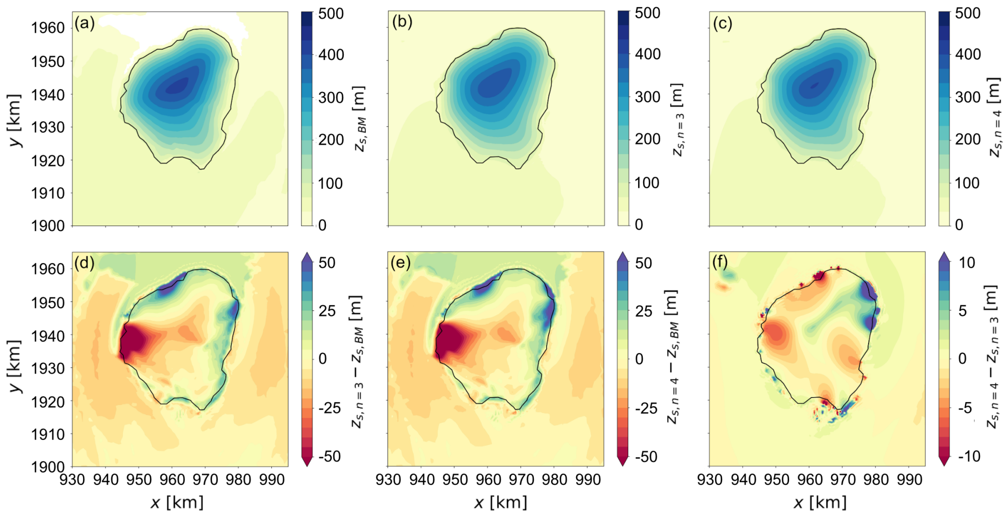

Figure 8. Surface elevation (a) from BedMachine Antarctica data, and (b) and (c) show the surface elevation of the $n = 3$ and $n = 4$ simulations, respectively, after the 400 year transient velocity spin up. The difference in surface elevation between the $n = 3$ simulation and the BedMachine data is shown in (d), the difference in surface elevation between the $n = 4$ simulation and the BedMachine data is shown in (e) and the difference in surface elevation between the $n = 4$ simulation and the $n = 3$ simulation is shown in (f). Note that (f) has a different colour scale than (d) and (e).

4.2 Comparisons between modelled and observed stratigraphy

Our new modelling framework allows us to further understand the similarities and differences between the observational data of Derwael Ice Rise and the simulated ice rise. Modelled isochrones are compared with dated isochrones derived from the radargrams obtained using airborne radar measurements. The radar measurements cover areas of Derwael Ice Rise including the ridge divide, flanks and grounding zones. The data is divided into seven cross-sections, each of which is compared with the model output for both $n = 3$ and $n = 4$ (Fig. 9). The modelled isochrones broadly reproduce the observed isochrones. The largest discrepancies between modelled and observed stratigraphy correspond to regions of the domain where the modelled and observed surface geometry do not match. For example, due to the tendency of the ice rise to broaden and thicken at the grounding zones and decrease in elevation in the centre during transient evolution, the elevation of the isochrones in these regions is generally under-estimated in the centre of the ice rise and over-estimated in the grounding zones. Evidence for this is provided by the cross-section $A{-}A'$ (Fig. 9a). There is a significant mismatch of up to 50 m between the modelled and observed isochrones, particularly on the eastern side which is likely due to an incorrect bed elevation. Mismatches with similar characteristics are also present in cross-sections $B - B'$, $C - C'$ and $F - F'$.

Fig. 10 shows the difference between the observed and modelled $n = 3$ isochronal slope for the cross-sections $A{-}A'$ to $F{-}F'$ in Fig. 1. Generally, the slopes of the modelled isochrones match well with the observed isochronal slopes. Areas where there is a close match between observed and modelled isochrones are indicated by white in Fig. 10. At all grounding lines around the ice rise, there is significant steepening of isochrones due to the downward motion of ice. Given the general tendency of the ice rise to broaden in the grounding zones, the steepening of the modelled isochrones tend to be located a small distance from the observed isochrones, but reproduce similar patterns in isochrone geometry. On the stoss side of the ice rise, thinning of the stratigraphy indicates sudden acceleration of ice a few kilometres away from the grounding line. This is particularly evident in the cross-sections $A - A'$.

In the observational data, the Raymond arch at the ridge divide is visible in the cross-sections $B{-}B'$, $C{-}C'$, $F{-}F'$ and $G{-}G'$. The side arch identified in Drews et al. (2015) is also visible in the cross-section $F{-}F'$. In Fig. 9e, the side arch visible in the observed isochrones is noticeable at a depth corresponding to the first modelled isochrone below the surface, which has an age of 100 years.

4.3 Velocities and strain rates

Simulated ice-shelf velocities on the western side of the ice rise are over 300 ma^{-1} and roughly 200 ma^{-1} on the eastern side. This is because of the location of the tributary Western Ragnhild Glacier. The asymmetry of the surrounding ice shelf results in an asymmetry in the divergence of the flow of ice around the ice rise. The simulated velocity field of the ice rise shows a distinct ridge divide on the northern side of the ice rise, with the divide positioned diagonally from the north east to the south west.

Absolute surface velocity differences between the $n = 3$ and the $n = 4$ simulations are generally below 10 % with the exception of the divide and the north-eastern and south-eastern sides of the ice rise (Fig. **??** in the Supporting Information). The largest negative velocity differences occur in north-eastern and south-eastern sides of the ice rise with higher velocities in the $n = 3$ simulation. In the talwegs, velocities are higher in the $n = 4$ simulation. Note that talweg is a term first introduced in relation to ice rises in Gillet-Chaulet et al. (2011) and is a geomorphological term describing a valley. At the ridge divide, the velocities are significantly lower in the $n = 4$ simulation than the $n =$ 3 simulation. In the areas perpendicular to the centre of the ridge divide, the $n = 4$ simulation has higher velocities than the $n = 3$ simulation. Elsewhere, the $n = 3$ sim-

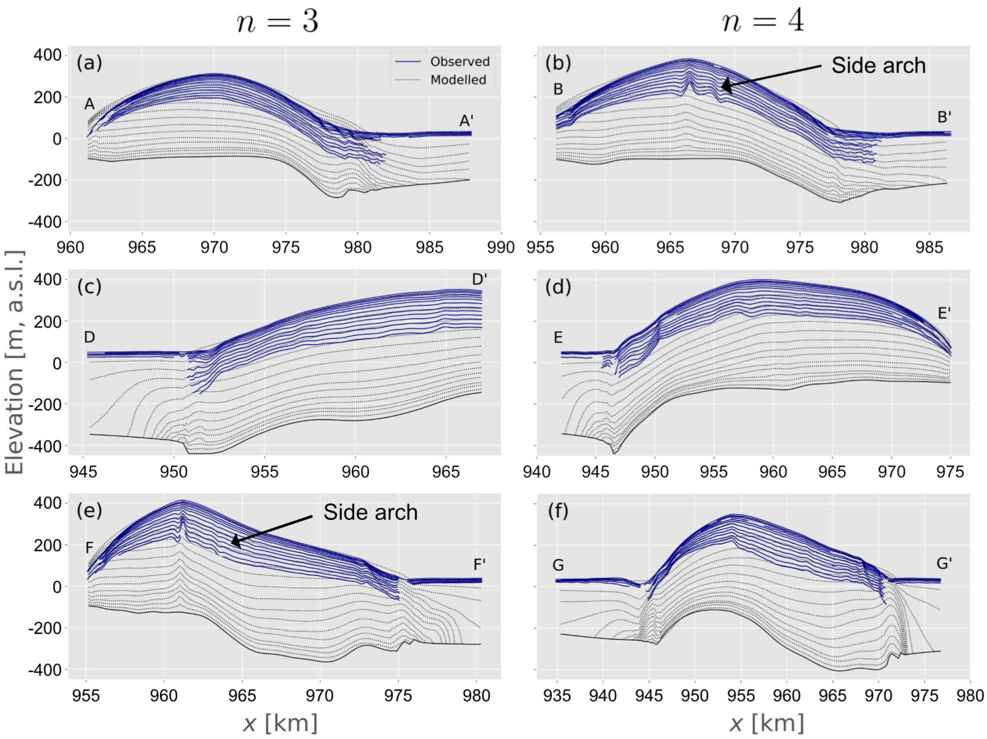

Figure 9. Comparisons between modelled and observed stratigraphy along radar profiles marked in 1 in the vertical domain of the model. Graphs in left columns, (a), (c), and (e), show comparisons for a Glen's flow law exponent of $n = 3$ (cross-sections $A - A'$, $D - D'$ and $F - F'$), and the right column, (b), (d), and (f), show comparisons for a Glen's flow law exponent of $n = 4$ (cross-sections $B - B'$, $E - E'$ and $G - G'$). The blue solid lines show the observed stratigraphy and the dotted black lines show the modelled stratigraphy.

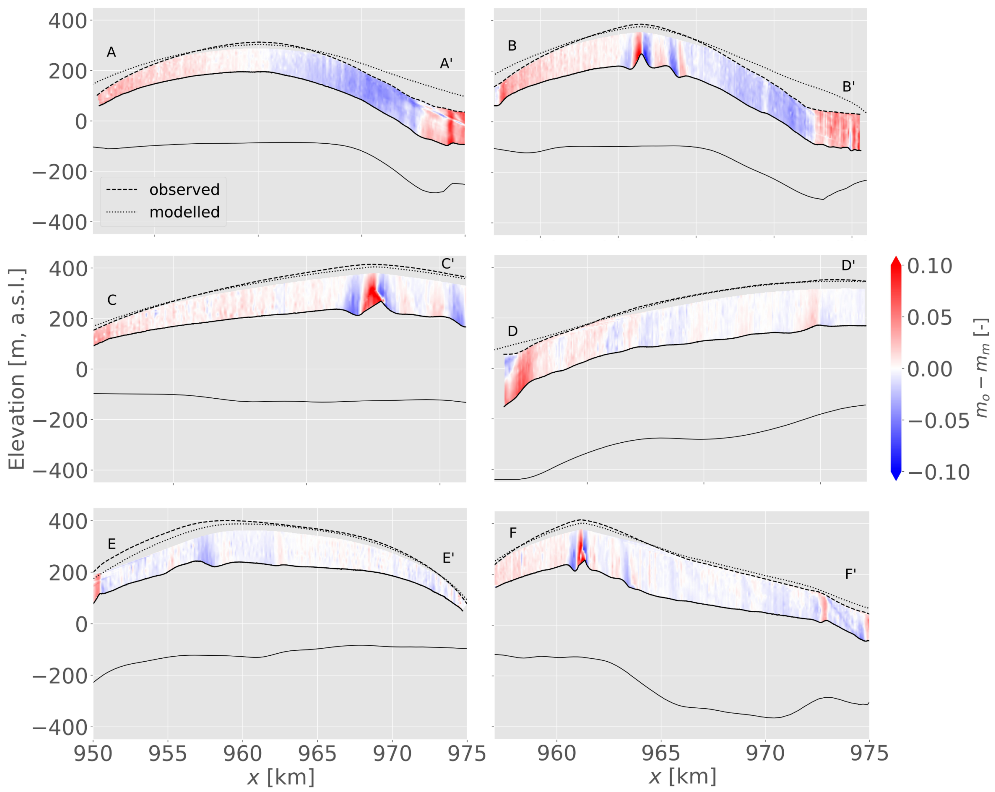

Figure 10. Difference between observed isochrone slope (m_o) and the $n = 3$ modelled isochrone slope (m_m) at locations where data is available for both. The cross-sections $A - A'$ to $F - F'$ correspond with the radar profiles in Fig. 1. The dashed lines show the observed ice surface and the dotted lines show the modelled surface. The lower extent of the area of comparison and the lower ice surface are shown with solid black lines.

ulation has higher velocities than the $n = 4$ simulation. A similar pattern of velocity difference between the $n = 3$ and the $n = 4$ simulations is observed at the depth of the 1000 year isochrone (Fig. **??** in the Supporting Information). Percentage differences in velocities are more pronounced in the talwegs at the 1000 year isochrone than at the ice surface. The flanks perpendicular to the ridge divide show higher velocities in the case of the $n = 4$ simulation than the $n = 3$ simulation. Furthermore, there are pronounced higher velocities in the $n = 3$ simulation in the south of the ice rise. Here, there is higher divergence of the velocity vectors (Fig. 12a), but not enough for an additional ridge or Raymond arches to form.

At the base of the ice rise, some basal sliding occurs. Lowest basal velocities of $<$ 1 ma^{-1} are simulated under the ridge divide and increase towards the flanks of the ice rise (Fig. **??**a in the Supporting Information). Interestingly, from the centre of the ice rise to the south-eastern corner, there is an area of low velocity compared with elsewhere in the flanks of the ice rise. In three locations in the grounded ice, close to the grounding line, there is a higher basal sliding velocity of 5 ma^{-1}. This indicates that there is a higher effective stress in these areas, leading to acceleration of the ice. In both the $n =$ 3 and $n = 4$ simulations, the same basal friction parameterisation is used, and so differences in the basal velocities are due to feedbacks with the overlying ice. A comparison of the basal velocities between the two simulations reveals that the largest differences are seen in the grounding zones, where basal velocities in the $n = 4$ simulation are higher than in the $n = 3$ simulation (Fig. **??**b in the Supporting Information). In the interior of the ice rise at the flanks of the ridge divide, velocities in the $n = 3$ simulation are higher than in the $n = 4$ simulation.

The computed ice surface shear strain rate in the direction of ice flow shows a similar pattern to the ice velocity. Higher shear strain rates are observed on the western side of the ice rise. These result from the larger velocities in the ice shelf (Fig. 11). On the eastern side of the ice rise, the shear strain rates are lower than on the western side. The areas of higher shear strain rate on the eastern side are concentrated in two areas; in the north east and the south east of the ice rise. The area of lower shear strain rate between the areas of higher shear strain rate are a consequence of velocities from the ice rise and ice shelf being more similar in magnitude. Differences in shear strain rates between the $n = 3$ and $n = 4$ simulations primarily occur on the western side of the ice rise. Differences on the eastern side of the ice rise are negligible in comparison and localised differences are likely due to slight differences in grounding line position.

Differences in ice velocity between the simulations also affect the computed internal stratigraphy. For both simulations, the oldest ice at a depth of 95 % is located at the ridge and on the stoss side of the ice rise. Here, convergence of flow from the ice rise and the ice shelf results in relatively stagnant ice velocities (Fig. **??** in the Supporting Information). The age field at a depth of 95 % shows that ice is on average 335 years older in the case of the $n = 3$ simulation. This reflects the higher strain rates and thus enhanced thinning of ice under a higher Glen's flow law exponent. At a depth of 50 %, differences in age are much less, with ice being between 25 and 50 years older at the divide in the case of the $n = 4$ simulation. The largest differences in age at a depth of 50 % are seen in the area of compression between the ice rise and the ice shelf and in the north-eastern corner of the ice rise, with ice being more than 50 years older in the case of the $n = 4$ simulation. The opposite is seen in the talwegs, where ice is older in the case of the $n = 3$ simulation at a depth of 50 %.

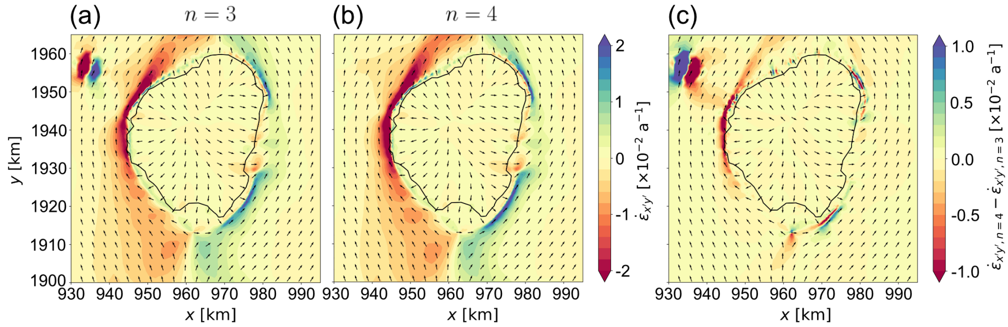

Figure 11. Shown in (a) and (b) is the shear strain rate for the $n = 3$ and $n = 4$ simulations, respectively, calculated by rotating the strain rate tensor to align with the velocity direction. In (c), the difference between the shear strain rate in the direction of the velocity of the $n = 4$ and $n = 3$ simulations is shown.

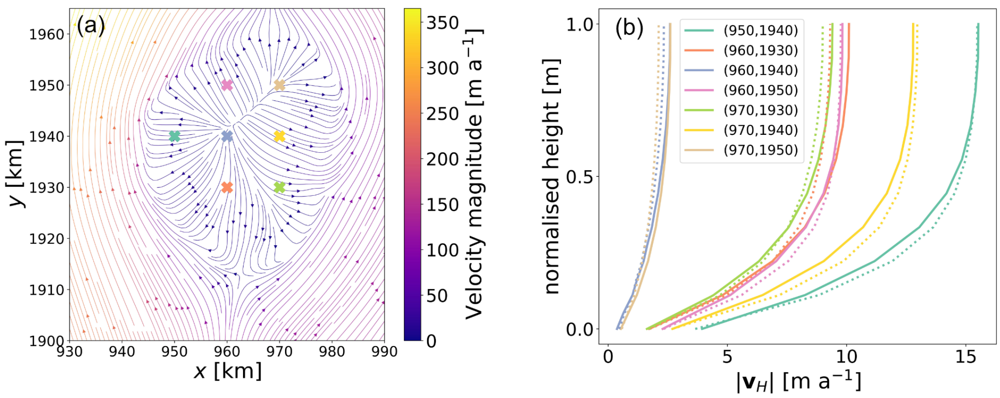

Figure 12. (a) shows the velocity field of Derwael Ice Rise, (b) shows the horizontal velocity magnitude for the (x, y) coordinates marked in (a), for the $n = 3$ simulation (solid lines) and the $n = 4$ simulation (dashed lines).

5 Discussion

5.1 Progress and challenges for three-dimensional ice rise modelling

Previous research has highlighted the importance of ice rises in deciphering past re-organisation of flow. Until now, the comparison between observed and modelled internal stratigraphy has been restricted to flow-line setups, providing a spatially limited assessment (Martín et al., 2006, 2009; Drews et al., 2015). We introduce a new three-dimensional modelling framework that overcomes these limitations and allows us to provide a spatially continuous age field that can be compared with radar observations. This provides an important step towards the routine simulation of ice rises and the ultimate goal of using them to constrain paleo ice-sheet simulations.

During the development of our modelling framework, we encountered a number of challenges. Given their small size, ice rises are often insufficiently resolved in continental-scale boundary datasets such as BedMachine or RACMO2.3p1. This can only be overcome if in-situ and high-resolution datasets are available to correct for these mismatches. The multiple steps necessary to spin-up the model are in parts subjective and a different sequence of spin-up steps of different simulation lengths may result in slightly differing results. As highlighted previously, it is important to note that interpolation errors in the bed elevation do occur and it may be necessary to make comparisons with the raw data. Failure to correct anomalies in the bed elevation data can result in artefacts in transient simulations, for example, a thickening of the ice rise after initialisation. This highlights the importance of such measurements to allow such studies for other ice rises around Antarctica.

The drift correction to the SMB implemented in our study results in an SMB field which is higher than the RACMO2.3p1 dataset (roughly 0.5 m a^{-1} higher) in the centre of the ice rise and lower closer to the margins of the ice rise than in the stratigraphy-adjusted SMB field. This points to a slight over-compensation of the ice softness and perhaps missing processes at the margins of the ice rise such as fracturing, higher melt rates or an anisotropic fabric or another process which would increase the velocity of the ice in that area. Another explanation is that the ice in the centre of the ice rise is stiffer in reality than in the model. As shown in Martín et al. (2009) and Martín and Gudmundsson (2012), anisotropic evolution of ice is a mechanism which enhances the stiffness of ice at an ice divide and the lack of this mechanism in our model is a likely reason for excess thinning of ice at the divide.

5.2 Comparison between modelled and observed stratigraphy

Much progress has been made in comparing modelled and observed internal stratigraphy (Sutter et al. (2021) and Born and Robinson (2021)) on large scales. For Stokes simulations, comparisons between modelled and observed stratigraphy have only been performed for two-dimensional simulations (Martín et al., 2009; Martín & Gudmundsson, 2012; Drews et al., 2015) and have so far not included the grounding line and the surrounding shelf. Including the ice shelf in the simulation domain means that grounding zone processes are included in the simulations and the domain boundaries are no longer within the bounds of the grounded area of the ice rise. Such a setup also allows investigation of isochrones in the shear zone between the ice rise and ice shelf which is characterised by steep isochrone geometries that are difficult to capture with radar observations.

The comparisons between the observed and modelled isochronal slopes in Fig. 10 show a close fit overall, with larger differences in the north east of the ice rise where issues with the bed elevation were found. Furthermore, differences are larger at the main Raymond arch where too coarse vertical resolution results in greater mismatches. Differences in isochrone slopes are primarily due to a mismatch in the surface elevation between modelled and observed results. The largest differences are seen in the north east of the ice rise and at the main Raymond arch and the side arch, which is not captured in the model. The side arch visible in the observed isochrones in Fig. 9e is visible at a depth corresponding to the first modelled isochrone below the surface which has an age of 100 years.

By studying areas where the surface elevation between the observed and modelled stratigraphy is similar, we can identify processes in ice dynamics which are not reproduced by the model. In cross-section $D{-}D'$, there is a deviation in isochrone slope at $x = 957$ km when comparing the modelled isochrones to the observed isochrones. A greater thinning of the isochrones in the observed stratigraphy indicates that the modelled ice may not adequately reproduce speed-up of the ice in this area. In the cross-section $G - G'$, the acceleration of ice seen in the observed stratigraphy is not reproduced to the same extent in the model on the western side of the cross-section. On the eastern side of the $G{-}G'$ cross-section, the modelled stratigraphy shows more gentle slopes than the observed stratigraphy, indicating that in the direction of the grounding zone, modelled ice is accelerating more than the observed ice.

The side arch marked in Fig. 9b was discussed in previous work and it was suggested that it may be a result of unresolved three-dimensional effects (Drews et al., 2015). The lack of a side arch in our three-dimensional simulations indicates that this is not the case and we instead hypothesise that Derwael Ice Rise was previously a triple junction ice rise and that a ridge was previously located where the side arch is seen in the observed stratigraphy. If this is the case, then a transition from a triple junction ice rise to a ridge divide ice rise is quite recent (¡ 100 years) as the side arches are also evident close to the surface. This then suggests that ice rises can have signatures of both ice-divide stability (evidenced by the oversized Raymond arches beneath the contemporary divide) and instability (evidenced by the side arch interpreted as a remnant of a ice-divide triple junction). Furthermore, it cannot be ruled out that the flow divide had switched more than once between the main arch and the side arch.

Comparing the modelled isochrones to the observed isochrones in the shear zone, we see that in the grounding zone, the observed isochrones steepen closer to the ice rise interior than the modelled isochrones. This is due to a grounding line advance in the simulations as a result of too little shear softening in the modelled shear zones around the ice rise, perhaps due to missing processes such as fracturing or an anisotropic fabric. An alternative approach to reducing the grounding line advance would be to alter the Arrhenius pre-factor to allow for softer ice, but this would result in a reduction of the ice rise elevation.

5.3 Glen's flow law exponent

In our study, we have investigated the influence of using a Glen's flow law exponent of $n = 3$ and $n = 4$. The $n = 4$ simulation results in a more peaked shape (Fig. 8). Both the $n = 3$ and the $n = 4$ simulations result in a slight lowering of the surface elevation in the ridge divide area, with the $n = 4$ simulation resulting in a surface elevation closer to that of the observed surface elevation. This is an indicator that a Glen's flow law exponent of $n = 4$ is more suitable, but a general tendency for excess thickening in the grounding zones means this result is not without uncertainty. The lower velocities in the $n = 4$ simulation compared with the $n = 3$ simulation align with our understanding of the Raymond effect, with lower velocities and greater Raymond arch amplitude associated with a higher Glen's flow law exponent. Interestingly, the differences in the flanks of the ice rise indicate different responses to the non-linearity that result in slight differences in flow regime.

Predicted age–depth relationships differ by < 5 % in most areas for simulations with $n = 3$ and $n = 4$ (Fig. **??** in the Supporting Information). This suggests that tuning of the Arrhenius factor and the drift-correction for the $n = 3$ and $n = 4$ simulations lead to similar velocity fields in both cases. Exceptions are the divide regions and the shear zones at the ice-rise boundaries where differences are significant. Larger differences are seen in areas where stresses are significantly higher or lower than average stresses. Strain rates in the ice are higher in the $n = 4$ than the $n = 3$ simulation in the shear zones and near the ice-bed interface. Despite these differences, the modelled stratigraphy does not differ significantly. Studies for which an appropriate Arrhenius factor for an exponent of $n = 4$ have so far only been performed with two-dimensional simulations (Martín et al., 2006; Drews et al., 2015), resulting in uncertainties due to the lack of through-plane velocities. A conversion of the Glen's flow law from an exponent of $n = 3$ to $n = 4$ is further complicated by the dependence of the Arrhenius law on the temperature, activation energy, and n itself. Notably, significant uncertainty exists within these parameters as they have been calibrated through few laboratory studies in specific conditions (Zeitz et al., 2020). In our conversion, we neglect differences in activation energies and use a typical stress, $[\tau_0]$, to calculate an initial guess for an appropriate Arrhenius Law for $n = 4$. This simplified scaling is useful as we are able to compare parameters within our model to observed stratigraphy, highlighting the most appropriate values for the flow law. The chosen typical stress is within a reasonable range as in Goldsby and Kohlstedt (2001) and Goldsby (2006). In conjunction with known uncertainties in our understanding of the kinetics of glacier ice, implies that constraints on mechanisms such as temperature, activation energy, and grain size implicit within the Arrhenius relation are necessary to better understand the kinetics of creep on natural glacier ice.

Due to the assumption that ice is incompressible, the horizontal dilation (Fig. **??** in the Supporting Information) is the equivalent of the vertical strain rate, $\dot{\varepsilon}_{zz}$, with a sign change. We assume that differences in strain rate with and without a firn column do not differ greatly. The higher horizontal dilation in the north-western and eastern talwegs in the $n = 4$ simulation than the $n = 3$ simulation implies that there is greater stretching occurring in the ice. The opposite effect is seen in the vicinity of the ice rise ridge divide, with a lower dilation in the case of the $n = 4$ simulation. These small-scale results, which are in agreement with those presented in Gillet-Chaulet et al. (2011), are an analogy for larger scale situations. On larger scales, the higher dilation in areas of high velocity is likely to have consequences for the timing of the onset of an ice stream. Interestingly, in our simulations of Derwael Ice Rise, the south-western region of the ice rise shows a large area where the dilation is lower in the case of the $n = 4$ simulation than the $n = 3$ simulation, resulting in a region which does not contain a ridge divide, but also does not have strain rate differences which one would expect in the talweg of an ice rise. These characteristics are indicative of an ice rise which is in a state close to having a triple junction flow regime. Furthermore, the spatial variation in dilation and the resulting change in distance between isochrones could help in future to determine a correct Glen's flow law exponent.

In Fig. 11, it can be seen that there are higher shear strain rates in the direction of flow in the shear margins in the case of the $n = 4$ simulation than in the $n = 3$ simulation. This result implies softer ice in shear margins when using a $n = 4$ simulation, indicative of viscous deformation at the higher strain rates. When investigating threshold shear strain rates or shear stresses beyond which fracturing occurs, it is important to bear in mind that a differing Glen's flow law exponent will have a differing effect in simulations. An important observation is that the ice rumple north-west of Derwael Ice Rise becomes less grounded in the case of the $n = 4$ simulation, which we attribute to the greater strain-rate softening of the ice for the higher Glen's flow law exponent. This has consequences for simulations including pinning points as the choice of Glen's flow law exponent may have an influence on the buttressing due to that pinning point. Moreover, the higher flux of ice into the ice shelf coming from the talweg on the eastern side of Derwael Ice Rise, results in low shear strain rates in the grounding zone compared with the shear zones upstream and downstream.

5.4 Model limitations and future research directions

We have assumed that Derwael Ice Rise is in steady state and have found parameter values which result in a steady-state geometry close to the present-day observed geometry. Extra care would need to be taken when modelling other ice rises which do not satisfy the steady-state criterion. The boundary and initial conditions of our model are dependent on both observational data and model output (from regional atmospheric climate model RACMO2.3p1). It is important to check for interpolation errors using the raw data. Failure to correct for the bed elevation led to a series of flawed transient simulations in our case. Furthermore, we have not coupled anisotropy evolution to our model as there is insufficient anisotropy data available to constrain the model. Inclusion of ice-anisotropy will increase Raymond arch amplitudes. In future work, three-dimensional ice rises will provide ideal locations for the analysis of differing anisotropy schemes as well as other physical processes such as ice fracture in the shear margins.

Ice rises are good locations to study the effect of ice flow parameters across different flow regimes. The isochronal patterns observed near the base and surface are directly linked to the SMB and BMB fields. Simply adjusting the SMB and BMB fields using the change in surface elevation after initialisation does not, however, suffice for inferring the correct boundary conditions. We have therefore first adjusted A and n in the Glen's flow law (J. Glen, 1958). The parameter n has an influence on the proportions of the dome shape of the ice rise as shown in, for example, Gillet-Chaulet et al. (2011). A range of Arrhenius factors, A, then need to be tested with the various Glen's flow law exponents, n, in order to obtain an optimal ice rise geometry. A further source of uncertainty is in the basal friction parameterisation. Assuming that there is negligible basal sliding where there is substantial horizontal divergence of ice flow, an adjustment of the basal friction parameter can be made until there is sufficient thinning of ice in the talweg and no thinning elsewhere. We acknowledge that although we aim to independently adjust the ice flow parameterisations and boundary conditions they are none-the-less dependent on one-another. We argue, however, that with the steps we have taken in model calibration and comparison with isochrones, we have moved a step closer to independently determining model parameters.

6 Conclusions

We have introduced a new three-dimensional ice-rise modelling framework that includes an ice rise, a grounding line, and the surrounding ice shelf. This framework allows us to compare the modelled three-dimensional stratigraphy with the observed stratigraphy. The modelling framework presented here can be transferred as is to other ice rises of interest to predict the age-depth fields prior to ice-core drilling and also to continue constraining ice-flow parameters relevant for continent-wide simulations. Overall, we find that the modelled stratigraphy of Derwael Ice Rise matches well with observed stratigraphy except in regions where there is uncertainty in the bed elevation. We predict 8000 year old ice at 95 % depth and spatial age gradients at intermediate depth are significant reflecting the spatial variability in SMB. Observed arches in the ice-rise flanks cannot be reproduced and are likely a remnant of a former ice-divide triple junction that has disappeared in the last 100 years.

The presented modelling framework provides a blueprint for the simulation of other ice rises with Glen's flow exponents of $n = 3$ and $n = 4$ to make comparisons with ice cores or observational stratigraphy with the hopes of narrowing down uncertainties in other model parameters in the future, such as temperature and grain size. Simulations with differing $n = 3$ and $n = 4$ broadly result in similar velocity and age-depth fields if the temperature dependent viscosity factors are tuned accordingly. Exceptions are areas close to the ice divide, the peripherial shear zones and in the ice close to the ice-bed interface, helping to establish limits on the strain rates that permit viscous flow. Furthermore, this framework is a valuable first step towards testing and constraining various physical processes such as fracturing and anisotropy, perhaps constrained with quad-polarimetric radar measurements (Ershadi et al., 2022).

Open Research Section

The code for the simulations can be found at `https://github.com/henryclara/Derwael/` and the code to produce the figures in the paper can be found at `https://github.com/henryclara/DerwaelAccompanyingCode`. The data for producing the figures and the data used as input to the model can be found at `https://nc-geophysik.guz.uni-tuebingen.de/index.php/s/7PdWiGeFJdFGMKH`.

Acknowledgments

C. Henry was supported by the Deutsche Forschungsgemeinschaft (DFG) in the framework of the priority programme 1158 ”Antarctic Research with comparative investigations in Arctic ice areas” by a grant SCHA 2139/1-1. C. Schannwell was supported by the German Federal Ministry of Education and Research (BMBF) as a Research for Sustainability initiative (FONA) through the PalMod project under the grant number 01LP1915C. R. Drews and V. Višnjević were supported by an Emmy Noether Grant of the Deutsche Forschungsgemeinschaft (DR 822/3-1). This work used resources of the Deutsches Klimarechenzentrum (DKRZ) granted by its Scientific Steering Committee (WLA) under project ID bm1164.

References

Bons, P. D., Jansen, D., Mundel, F., Bauer, C. C., Binder, T., Eisen, O., … others (2016). Converging flow and anisotropy cause large-scale folding in greenland’s ice sheet. *Nature communications*, *7*(1), 1–6.

Bons, P. D., Kleiner, T., Llorens, M.-G., Prior, D. J., Sachau, T., Weikusat, I., & Jansen, D. (2018). Greenland ice sheet: Higher nonlinearity of ice flow significantly reduces estimated basal motion. *Geophysical Research Letters*, *45*(13), 6542–6548.

Born, A., & Robinson, A. (2021). Modeling the greenland englacial stratigraphy. *The Cryosphere*, *15*(9), 4539–4556.

Budd, W., & Jacka, T. (1989). A review of ice rheology for ice sheet modelling. *Cold Regions Science and Technology*, *16*(2), 107-144. Retrieved from `https://www.sciencedirect.com/science/article/pii/0165232X89900141` doi: https://doi.org/10.1016/0165-232X(89)90014-1

Callens, D., Drews, R., Witrant, E., Philippe, M., & Pattyn, F. (2016, June). Temporally stable surface mass balance asymmetry across an ice rise derived from radar internal reflection horizons through inverse modeling. *Journal of Glaciology*, *62*(233), 525–534. Retrieved 2022-01-13, from `https://www.cambridge.org/core/product/identifier/S0022143016000411/type/journal_article` doi: 10.1017/jog.2016.41

Callens, D., Matsuoka, K., Steinhage, D., Smith, B., Witrant, E., & Pattyn, F. (2014, May). Transition of flow regime along a marine-terminating outlet glacier in East Antarctica. *The Cryosphere*, *8*(3), 867–875. Retrieved 2021-11-21, from `https://tc.copernicus.org/articles/8/867/2014/` doi: 10.5194/tc-8-867-2014

Cavitte, M. G., Goosse, H., Wauthy, S., Kausch, T., Tison, J.-L., Van Liefferinge, B., … Claeys, P. (2022). From ice core to ground-penetrating radar: representativeness of smb at three ice rises along the princess ragnhild coast, east antarctica. *Journal of Glaciology*, *68*(272), 1221–1233. doi: 10.1017/jog.2022.39

Comiso, J. C. (2000, May). Variability and trends in antarctic surface temperatures from in situ and satellite infrared measurements. *Journal of Climate*, *13*(10), 1674–1696. Retrieved from `http://journals.ametsoc.org/doi/10.1175/1520-0442(2000)013<1674:VATIAS>2.0.CO;2` doi: 10.1175/1520-0442(2000)013⟨1674:VATIAS⟩2.0.CO;2

Drews, R., Matsuoka, K., Martín, C., Callens, D., Bergeot, N., & Pattyn, F. (2015, March). Evolution of Derwael Ice Rise in Dronning Maud Land, Antarctica, over the last millennia. *Journal of Geophysical Research: Earth Surface*, *120*(3), 564–579. Retrieved 2021-08-16, from `http://doi.wiley.com/10.1002/2014JF003246` doi: 10.1002/2014JF003246

Drews, R., Schannwell, C., Ehlers, T., Gladstone, R., Pattyn, F., & Matsuoka, K. (2020). Atmospheric and oceanographic signatures in the ice shelf channel morphology of roi baudouin ice shelf, east antarctica, inferred from radar data. *Journal of Geophysical Research: Earth Surface*, *125*(7), e2020JF005587.

Ershadi, M. R., Drews, R., Martín, C., Eisen, O., Ritz, C., Corr, H., … Mulvaney, R. (2022). Polarimetric radar reveals the spatial distribution of ice fabric at domes and divides in east antarctica. *The Cryosphere*, *16*(5), 1719–1739. Retrieved from `https://tc.copernicus.org/articles/16/1719/2022/` doi: 10.5194/tc-16-1719-2022

Favier, L., & Pattyn, F. (2015, June). Antarctic ice rise formation, evolution, and stability. *Geophysical Research Letters*, *42*(11), 4456–4463. Retrieved 2021-08-16, from `https://onlinelibrary.wiley.com/doi/abs/10.1002/2015GL064195` doi: 10.1002/2015GL064195

Favier, L., Pattyn, F., Berger, S., & Drews, R. (2016, November). Dynamic influence of pinning points on marine ice-sheet stability: a numerical study in Dronning Maud Land, East Antarctica. *The Cryosphere*, *10*(6), 2623–2635. Retrieved 2021-12-09, from `https://tc.copernicus.org/articles/10/2623/2016/` doi: 10.5194/tc-10-2623-2016

Franke, S., Bons, P. D., Westhoff, J., Weikusat, I., Binder, T., Streng, K., … others (2022). Holocene ice-stream shutdown and drainage basin reconfiguration in northeast greenland. *Nature Geoscience*, 1–7.

Gagliardini, O., Zwinger, T., Gillet-Chaulet, F., Durand, G., Favier, L., de Fleurian, B., … Thies, J. (2013, August). Capabilities and performance of Elmer/Ice, a new-generation ice sheet model. *Geoscientific Model Development*, *6*(4), 1299–1318. Retrieved 2021-08-16, from `https://gmd.copernicus.org/articles/6/1299/2013/` doi: 10.5194/gmd-6-1299-2013

Gillet-Chaulet, F., & Hindmarsh, R. C. (2011). Flow at ice-divide triple junctions: 1. three-dimensional full-stokes modeling. *Journal of Geophysical Research: Earth Surface*, *116*(F2).

Gillet-Chaulet, F., Hindmarsh, R. C. A., Corr, H. F. J., King, E. C., & Jenkins, A. (2011, December). *In-situ* quantification of ice rheology and direct measurement of the Raymond Effect at Summit, Greenland using a phase-sensitive radar. *Geophysical Research Letters*, *38*(24), n/a–n/a. Retrieved 2021-11-21, from `http://doi.wiley.com/10.1029/2011GL049843` doi: 10.1029/2011GL049843

Glen, J. (1958). The flow law of ice: A discussion of the assumptions made in glacier theory, their experimental foundations and consequences. *IASH Publ*, *47*(171), e183.

Glen, J. W. (1955). The creep of polycrystalline ice. *Proceedings of the Royal Society of London. Series A. Mathematical and Physical Sciences*, *228*(1175), 519–538.

Goel, V., Martín, C., & Matsuoka, K. (2018). Ice-rise stratigraphy reveals changes in surface mass balance over the last millennia in dronning maud land. *Journal of*

Glaciology, *64*(248), 932–942. doi: 10.1017/jog.2018.81

Goldsby, D. L. (2006). Superplastic flow of ice relevant to glacier and ice-sheet mechanics. *Glacier science and environmental change*, 308–314.

Goldsby, D. L., & Kohlstedt, D. L. (2001). Superplastic deformation of ice: Experimental observations. *Journal of Geophysical Research: Solid Earth*, *106*(B6), 11017–11030.

Henry, A. C. J., Drews, R., Schannwell, C., & Višnjević, V. (2022). Hysteretic evolution of ice rises and ice rumples in response to variations in sea level. *The Cryosphere*, *16*(9), 3889–3905. Retrieved from `https://tc.copernicus.org/articles/16/3889/2022/` doi: 10.5194/tc-16-3889-2022

Hindmarsh, R. C., King, E. C., Mulvaney, R., Corr, H. F., Hiess, G., & Gillet-Chaulet, F. (2011). Flow at ice-divide triple junctions: 2. three-dimensional views of isochrone architecture from ice-penetrating radar surveys. *Journal of Geophysical Research: Earth Surface*, *116*(F2).

Jezek, K. C. (2003). Observing the antarctic ice sheet using the radarsat-1 synthetic aperture radar. *Polar Geography*, *27*(3), 197-209. Retrieved from `https://doi.org/10.1080/789610167` doi: 10.1080/789610167

Koch, I., Drews, R., Franke, S., Jansen, D., Oraschewski, F. M., Muhle, L., . . . Eisen, O. (n.d.). Radar internal reflection horizons from multisystem data reflect ice dynamic and surface accumulation history along the princess ragnhild coast, dronning maud land, east antarctica [in review]. *Journal of Glaciology*.

Koch, I., Drews, R., Muhle, L. S., Franke, S., Jansen, D., Oraschewski, F., . . . Eisen, O. (n.d.). Internal reflection horizons of ice shelves and ice rises in eastern dronning maud land (east antarctica) from multisystem radio-echo sounding data [in review]. *PANGAEA*. doi: https://doi.pangaea.de/10.1594/PANGAEA.950383

Martín, C., & Gudmundsson, G. H. (2012). Effects of nonlinear rheology, temperature and anisotropy on the relationship between age and depth at ice divides. *The Cryosphere*, *6*(5), 1221–1229. Retrieved from `https://tc.copernicus.org/articles/6/1221/2012/` doi: 10.5194/tc-6-1221-2012

Martín, C., Gudmundsson, G. H., & King, E. C. (2014). Modelling of Kealey Ice Rise, Antarctica, reveals stable ice-flow conditions in East Ellsworth Land over millennia. *Journal of Glaciology*, *60*(219), 139–146. Retrieved 2021-08-16, from `https://www.cambridge.org/core/product/identifier/S0022143000203286/type/journal_article` doi: 10.3189/2014JoG13J089

Martín, C., Hindmarsh, R. C. A., & Navarro, F. J. (2006). Dating ice flow change near the flow divide at Roosevelt Island, Antarctica, by using a thermomechanical model to predict radar stratigraphy. *Journal of Geophysical Research*, *111*(F1), F01011. Retrieved 2021-08-16, from `http://doi.wiley.com/10.1029/2005JF000326` doi: 10.1029/2005JF000326

Martín, C., Hindmarsh, R. C. A., & Navarro, F. J. (2009, April). On the effects of divide migration, along-ridge flow, and basal sliding on isochrones near an ice divide. *Journal of Geophysical Research*, *114*(F2), F02006. Retrieved 2021-08-16, from `http://doi.wiley.com/10.1029/2008JF001025` doi: 10.1029/2008JF001025

Millstein, J. D., Minchew, B. M., & Pegler, S. S. (2022). Ice viscosity is more sensitive to stress than commonly assumed. *Communications Earth & Environment*, *3*(1), 1–7.

Morlighem, M., Rignot, E., Binder, T., Blankenship, D., Drews, R., Eagles, G., . . . others (2020). Deep glacial troughs and stabilizing ridges unveiled beneath the margins of the antarctic ice sheet. *Nature Geoscience*, *13*(2), 132–137.

Nereson, N. A., Raymond, C. F., Waddington, E. D., & Jacobel, R. W. (1998). Migration of the siple dome ice divide, west antarctica. *Journal of Glaciology*, *44*(148), 643–652. Retrieved from `https://www.cambridge.org/core/product/identifier/S0022143000002148/type/journal_article` doi:

10.3189/S0022143000002148

Philippe, M., Tison, J.-L., Fjøsne, K., Hubbard, B., Kjær, H. A., Lenaerts, J., ... others (2016). Ice core evidence for a 20th century increase in surface mass balance in coastal dronning maud land, east antarctica. *The Cryosphere*, *10*(5), 2501–2516.

Raymond, C. F. (1983). Deformation in the Vicinity of Ice Divides. *Journal of Glaciology*, *29*(103), 357–373. Retrieved 2021-08-16, from `https://www.cambridge.org/core/product/identifier/S0022143000030288/type/journal_article` doi: 10.1017/S0022143000030288

Rignot, J. M., E., & Scheuchl., B. (2017). *Measures insar-based antarctica ice velocity map, version 2.* NASA National Snow and Ice Data Center Distributed Active Archive Center. Retrieved from `https://nsidc.org/data/NSIDC-0484/versions/2` doi: 10.5067/D7GK8F5J8M8R

Ritz, C. (1987). *Time dependent boundary conditions for calculation of temperature fields in ice sheets. in: E. d. waddington and j. s. walder (eds.), the physical basis of ice sheet modelling, iahs publication no. 170, pp. 207–216.* IAHS Press, Wallingford, UK.

Schannwell, C., Drews, R., Ehlers, T. A., Eisen, O., Mayer, C., & Gillet-Chaulet, F. (2019, October). Kinematic response of ice-rise divides to changes in ocean and atmosphere forcing. *The Cryosphere*, *13*(10), 2673–2691. Retrieved 2021-11-21, from `https://tc.copernicus.org/articles/13/2673/2019/` doi: 10.5194/tc-13-2673-2019

Schannwell, C., Drews, R., Ehlers, T. A., Eisen, O., Mayer, C., Malinen, M., ... Eisermann, H. (2020, November). Quantifying the effect of ocean bed properties on ice sheet geometry over 40 000 years with a full-Stokes model. *The Cryosphere*, *14*(11), 3917–3934. Retrieved 2021-11-21, from `https://tc.copernicus.org/articles/14/3917/2020/` doi: 10.5194/tc-14-3917-2020

Sutter, J., Fischer, H., & Eisen, O. (2021). Investigating the internal structure of the antarctic ice sheet: the utility of isochrones for spatiotemporal ice-sheet model calibration. *The Cryosphere*, *15*(8), 3839–3860.

van den Broeke, M. R. (2019). *RACMO2.3p1 annual surface mass balance Antarctica (1979-2014)* [data set]. PANGAEA. Retrieved from `https://doi.org/10.1594/PANGAEA.896940` doi: 10.1594/PANGAEA.896940

Waddington, E. D., Neumann, T. A., Koutnik, M. R., Marshall, H.-P., & Morse, D. L. (2007). Inference of accumulation-rate patterns from deep layers in glaciers and ice sheets. *Journal of Glaciology*, *53*(183), 694–712. doi: 10.3189/002214307784409351

Weertman, J. (1957). On the sliding of glaciers. *Journal of Glaciology*, *3*(21), 33–38. doi: 10.3189/S0022143000024709

Weertman, J. (1983, May). Creep deformation of ice. *Annual Review of Earth and Planetary Sciences*, *11*(1), 215–240. Retrieved from `https://www.annualreviews.org/doi/10.1146/annurev.ea.11.050183.001243` doi: 10.1146/annurev.ea.11.050183.001243

Zeitz, M., Levermann, A., & Winkelmann, R. (2020). Sensitivity of ice loss to uncertainty in flow law parameters in an idealized one-dimensional geometry. *The Cryosphere*, *14*(10), 3537–3550.

Zwinger, T., Greve, R., Gagliardini, O., Shiraiwa, T., & Lyly, M. (2007). A full stokes-flow thermo-mechanical model for firn and ice applied to the gorshkov crater glacier, kamchatka. *Annals of Glaciology*, *45*, 29–37.

Zwinger, T., & Moore, J. C. (2009). Diagnostic and prognostic simulations with a full stokes model accounting for superimposed ice of midtre lovénbreen, svalbard. *The Cryosphere*, *3*(2), 217–229. Retrieved from `https://tc.copernicus.org/articles/3/217/2009/` doi: 10.5194/tc-3-217-2009

Supporting Information for "Predicting the three-dimensional age-depth field of an ice rise"

A. C. J. Henry[1,2,3], C. Schannwell[1], V. Višnjević[2], J. Millstein[4], P. D. Bons[2],

O. Eisen[5,6], R. Drews[2]

[1]Max Planck Institute for Meteorology, Hamburg, Germany

[2]Department of Geosciences, University of Tübingen, Tübingen, Germany

[3]International Max Planck Research School on Earth System Modelling, Max Planck Institute for Meteorology, Hamburg, Germany

[4]Massachusetts Institute of Technology—Woods Hole Oceanographic Institute Joint Program in Oceanography/Applied Ocean Science and Engineering, Cambridge, MA, USA

[5]Alfred Wegener Institute Helmholtz Centre for Polar and Marine Research, Bremerhaven, Germany

[6]University of Bremen, Bremen, Germany

Contents of this file

1. Figures S1 to S10

Introduction

The supporting information contains additional figures pertaining to the simulations described in the main article. Figures included show (1) the age at 50 and 95 % depth for the simulations using Glen's flow law exponents of $n = 3$ and $n = 4$, (2) the percentage difference in velocity magnitude at the surface and at the 1000 year isochrone for the $n = 3$ and $n = 4$ simulations, (3) the basal velocity magnitude for the $n = 4$ simulation and the difference in basal velocity magnitude between the $n = 3$ and $n = 4$ simulations, (4) the horizontal surface dilation for the $n = 3$ and $n = 4$ simulations and the difference between the two, (5) comparisons between RACMO2.3p1, stratigraphy-derived and drift-corrected surface mass balance (SMB) fields, (6) vertical temperature evolution profiles sampled at two coordinates, (7) comparisons between observed and modelled stratigraphy for all $n = 3$ and $n = 4$ simulation cross-sections not included in the main article and (8) the slope difference between the modelled and observed stratigraphy for the cross-section $G - G'$.

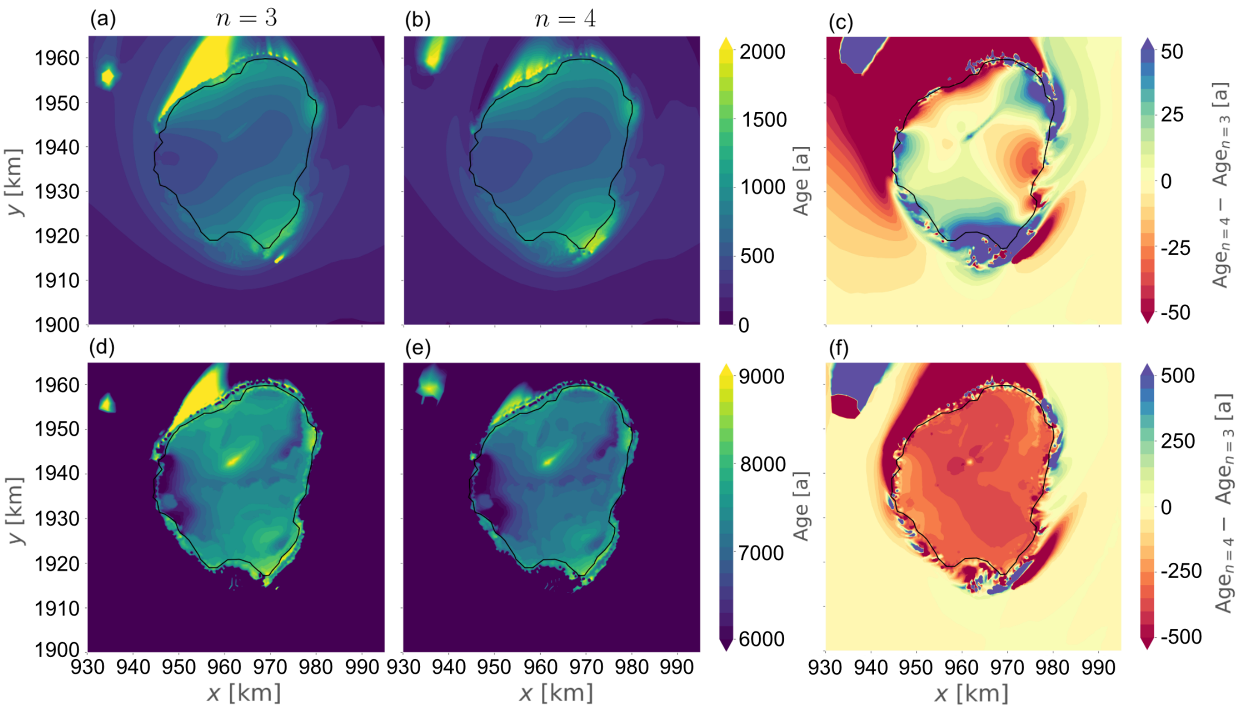

Figure S1. In (a) and (b), the age of the ice is shown at a depth of 50 % for the $n = 3$ and $n = 4$ simulations, respectively, and in (c), the difference between the $n = 4$ and the $n = 3$ simulations. In (d) and (e), the age of the ice is shown at a depth of 95 % for the $n = 3$ and $n = 4$ simulations, respectively. In (c) and (f), the difference between the age in the $n = 4$ and the $n = 3$ simulations is shown for a depth of 50 % and 95 %, respectively.

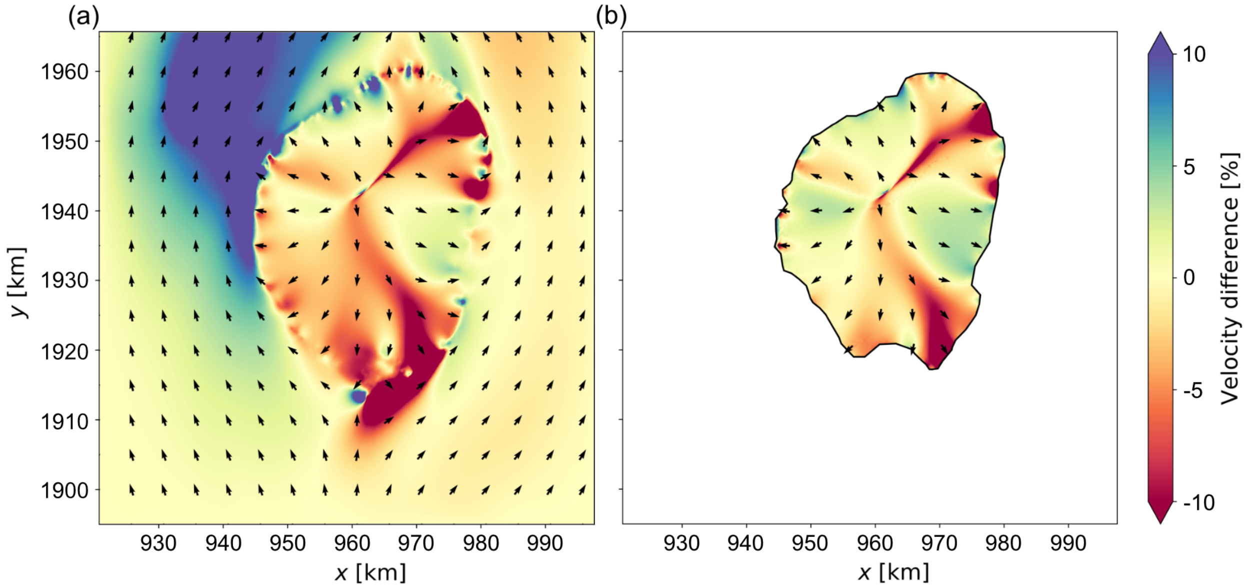

Figure S2. In (a), the percentage difference between the surface velocity magnitudes in the case of the $n = 4$ simulation and the $n = 3$ simulation. In (b), the percentage difference between the velocity magnitudes at the $Age = 1000$ a isochrone in the case of the $n = 4$ simulation and the $n = 3$ simulation. The arrows indicate the velocity directions of the $n = 3$ simulation. Note that the velocity magnitude of the $n = 3$ simulation is subtracted from the velocity magnitude of the $n = 4$ simulation.

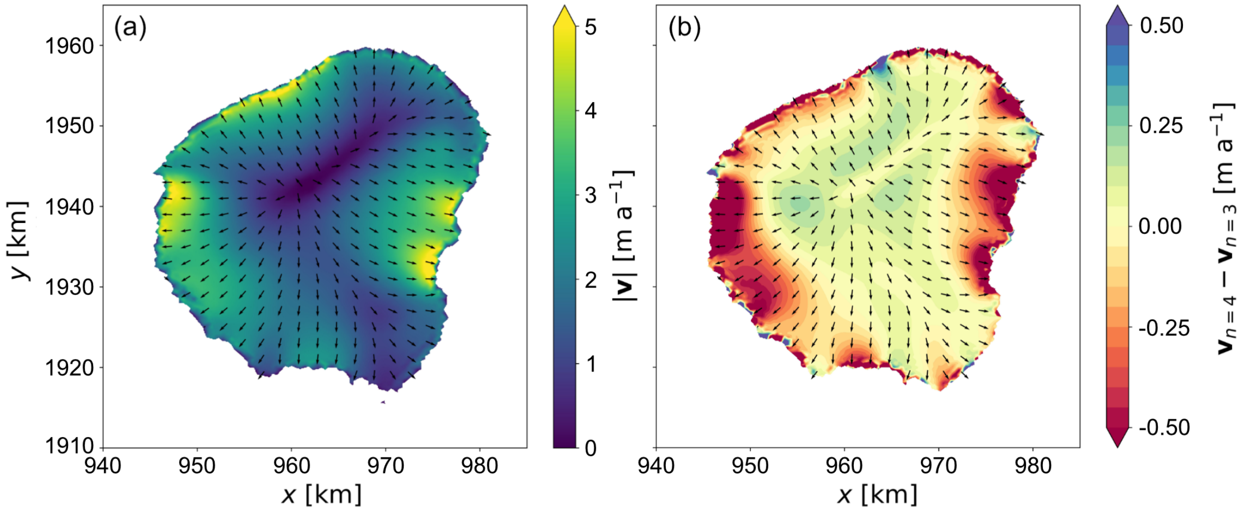

Figure S3. The basal velocity of the $n = 4$ simulation is shown in (a). The colour indicates the velocity magnitude and the arrows indicate the velocity direction. The basal velocity magnitude difference between the $n = 3$ and the $n = 4$ simulation is shown in (b). Note that the basal velocity magnitude of the $n = 3$ simulation is subtracted from the basal velocity magnitude of the $n = 4$ simulation.

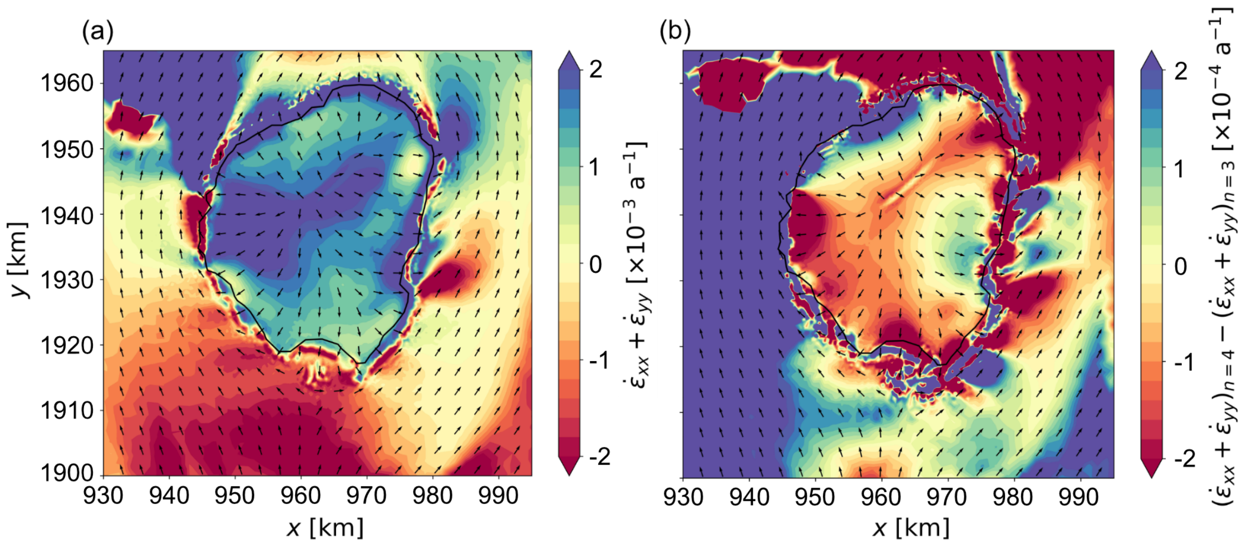

Figure S4. In (a), the horizontal dilation of the velocity field in the case of the $n = 3$ simulation is shown. In (b), the difference between the horizontal dilation in the case of the $n = 4$ and $n = 3$ simulations is shown. Note that the dilation of the $n = 3$ simulation is subtracted from the dilation of the $n = 4$ simulation.

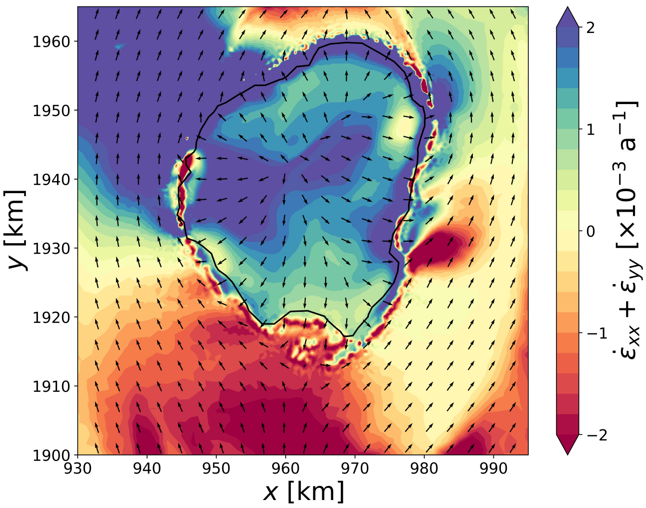

Figure S5. The horizontal dilation of the velocity field in the case of the $n = 4$ simulation.

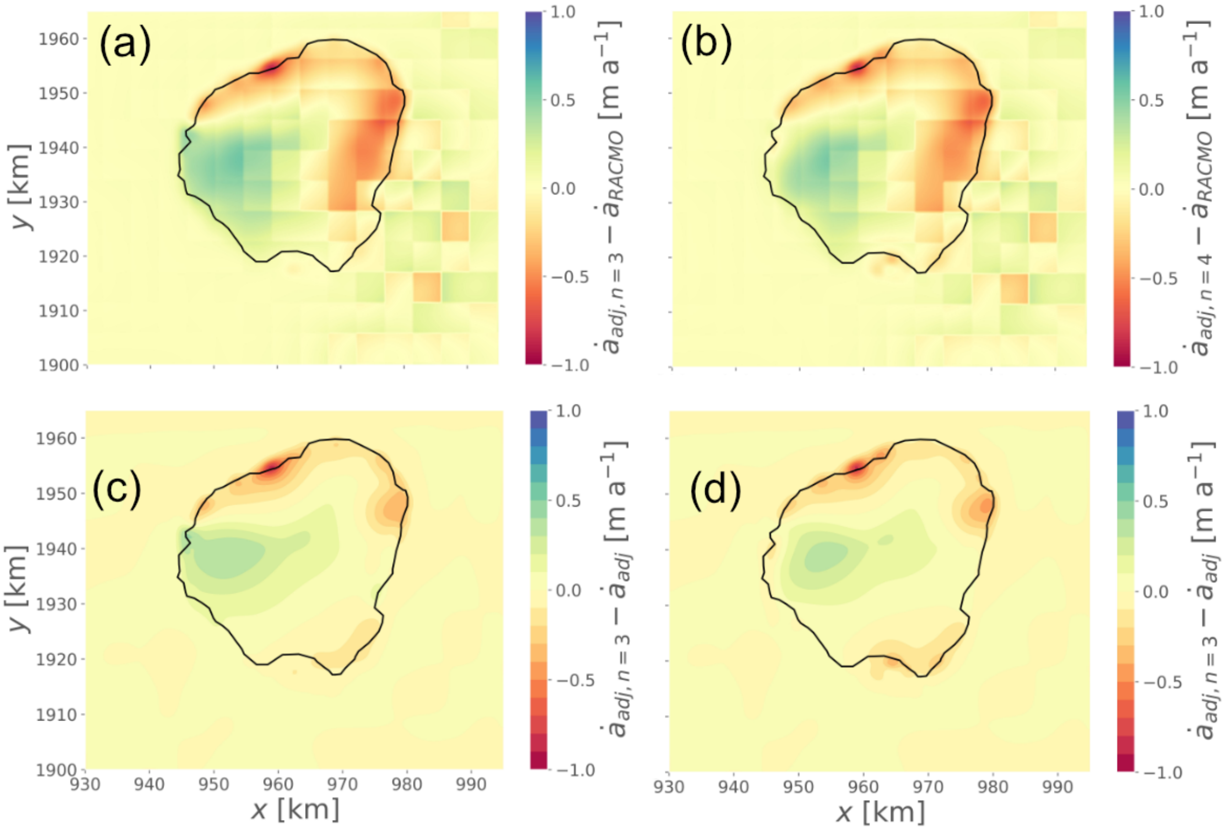

Figure S6. (a) and (b) show the difference between the SMB of the $n = 3$ and the RACMO2.3p1 data, and between the $n = 4$ simulations and the RACMO2.3p1 data , respectively. (c) and (d) show the difference between the SMB after and before the $\partial z_s/\partial t$ field adjustment for the simulations $n = 3$ and $n = 4$, respectively. Note: all SMB data is in ice-equivalent.

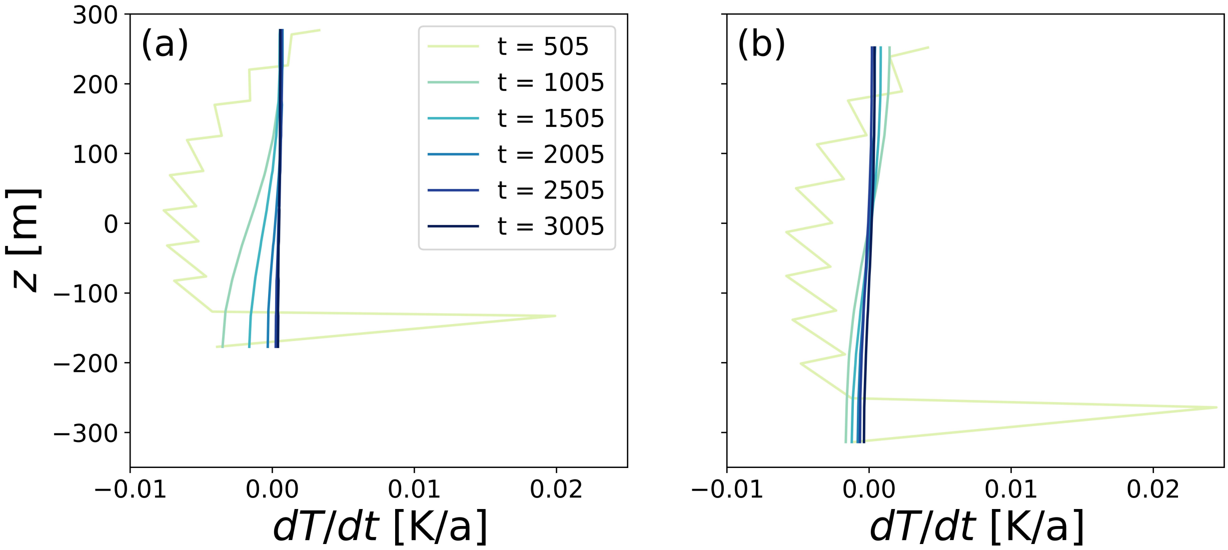

Figure S7. Figures (a) and (b) show the temperature evolution profiles at the horizontal coordinates $(x, y) = (970, 1940)$ and $(x, y) = (960, 1930)$, respectively, during the temperature spin up.

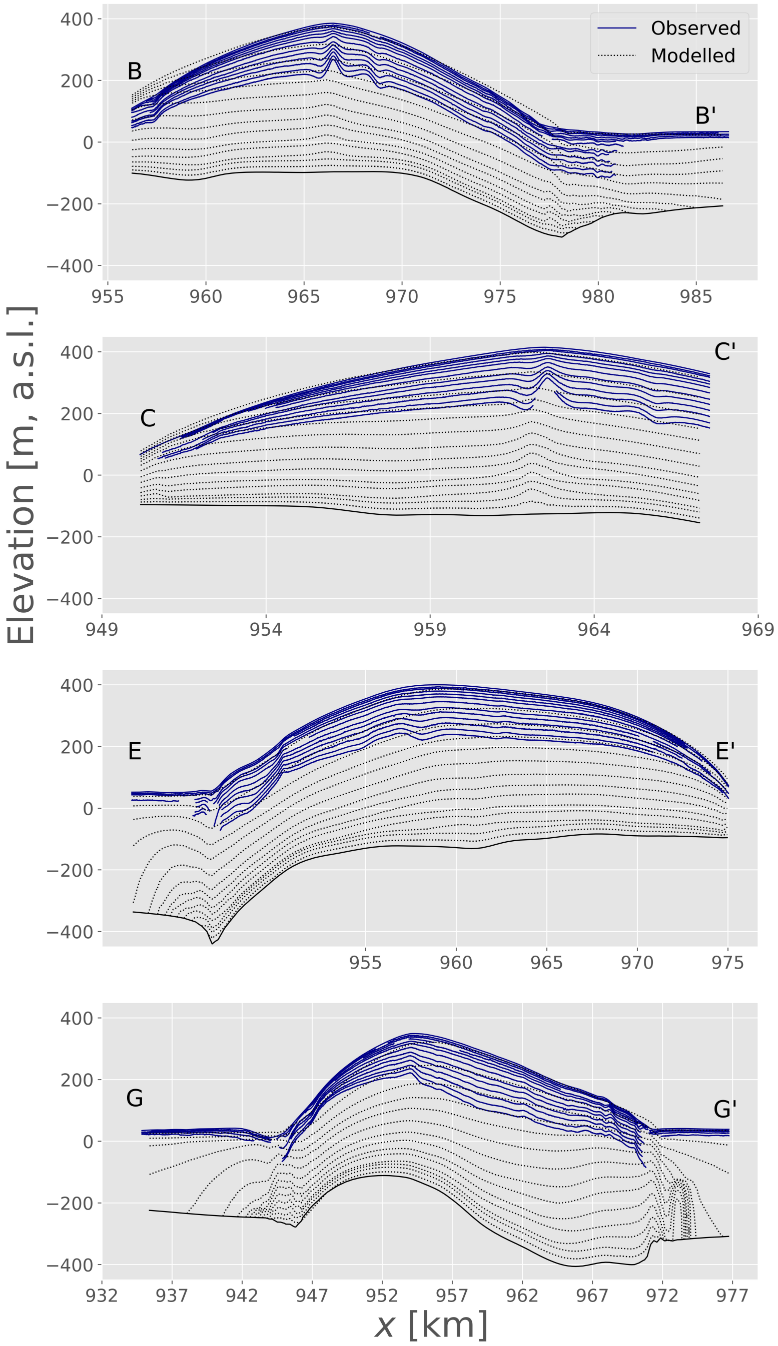

Figure S8. Comparisons between modelled and observed stratigraphy along radar profiles marked in **??** in the vertical domain of the model. Modelled isochrones correspond to the $n = 3$ simulation. The blue solid lines show the observed stratigraphy and the dotted black lines show the modelled stratigraphy.

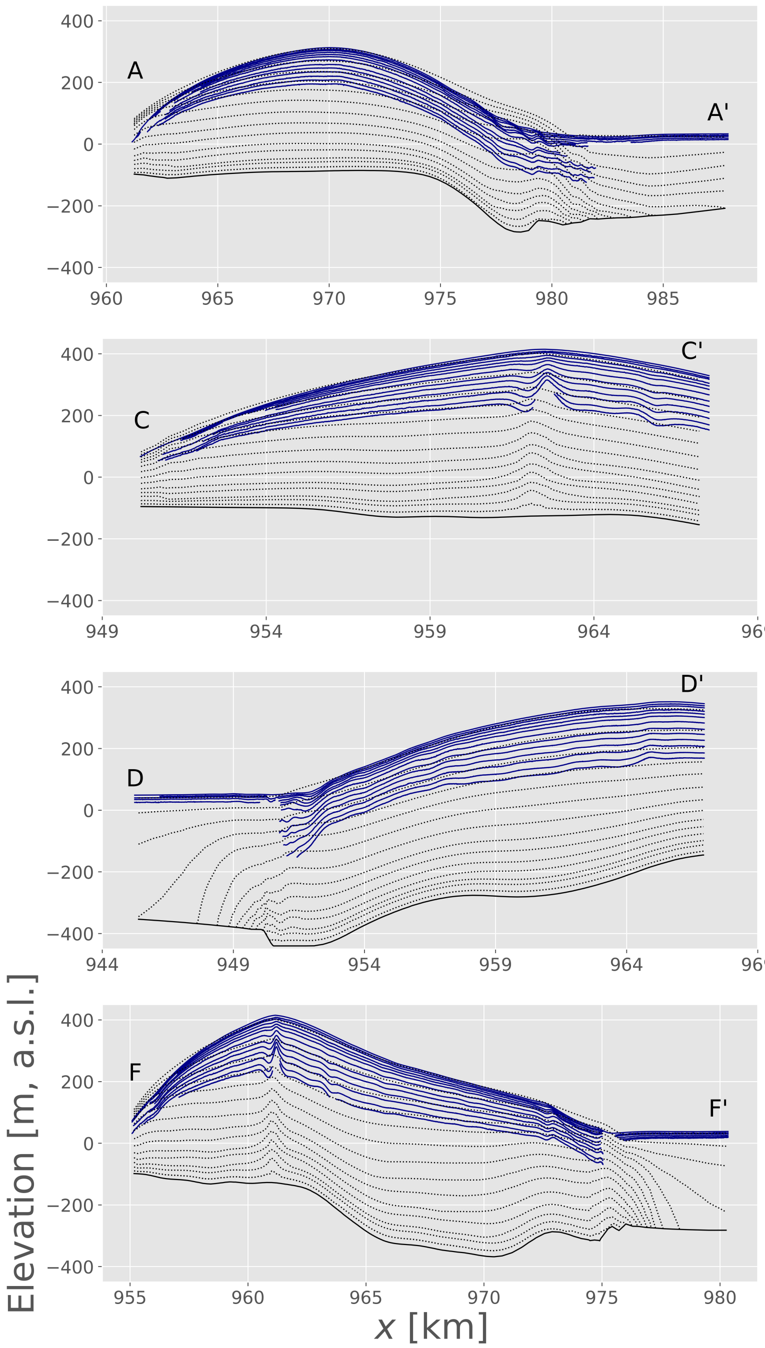

Figure S9. Comparisons between modelled and observed stratigraphy along radar profiles marked in **??** in the vertical domain of the model. Modelled isochrones correspond to the $n = 4$ simulation. The blue solid lines show the observed stratigraphy and the dotted black lines show the modelled stratigraphy.

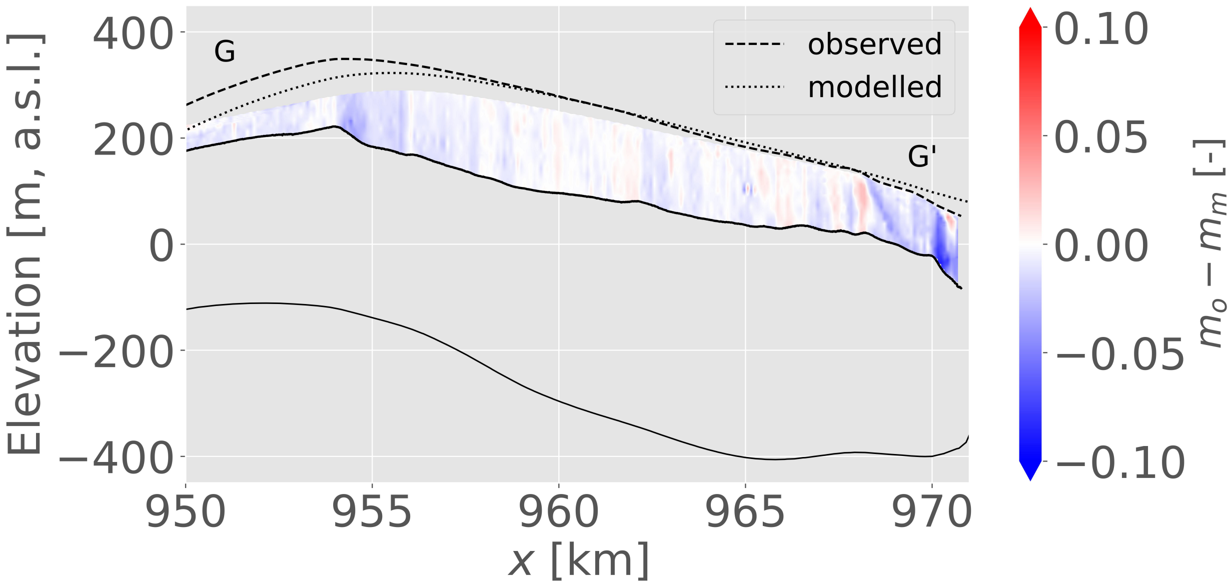

Figure S10. Difference between observed isochrone slope (m_o) and the $n = 3$ modelled isochrone slope (m_m) at locations where data is available for both. The cross-section $G - G'$ corresponds with the radar profile in Fig. 1 in the main article. The dashed lines show the observed ice surface and the dotted lines show the modelled surface. The lower extent of the area of comparison and the lower ice surface are shown with solid black lines.